On Utilizing Topology Optimization to Design Support Structure to Prevent Residual Stress Induced Build Failure in Laser Powder Bed Metal Additive Manufacturing

Lin Cheng[1], Xuan Liang[1], Jiaxi Bai[1], Qian Chen[1], John Lemon[2], Albert To[1*]

[1] Department of Mechanical Engineering and Materials Science, University of Pittsburgh, Pittsburgh, PA 15261

[2] Oberg Industries, 2301 Silverville Road, Freeport, PA 16229

Abstract: Metal additive manufacturing (AM) as an emerging manufacturing technique has been gradually accepted to manufacture end-use components. However, one of the most critical issues preventing its broad applications is build failure resulting from residual stress accumulation in manufacturing process. The goal of this work is to investigate the feasibility of using topology optimization to design support structure to mitigate residual stress induced build failure. To make topology optimization computationally tractable, the inherent strain method is employed to perform fast prediction of residual stress in an AM build. Graded lattice structure optimization is utilized to design the support structure due to the open-celled and self-supporting nature of periodic lattice structure. The objective for the optimization is to minimize the mass of sacrificial support structure under stress constraint. By limiting the maximum stress under the yield strength, cracking resulting from residual stress can be prevented. To show the feasibility of the proposed method, the support structure of a double-cantilever beam and a hip implant is designed, respectively. The support structure after optimization can achieve a weight reduction of approximately 60%. The components with optimized support structures no longer suffer from stress-induced cracking after the designs are realized by AM, which proves the effectiveness of the proposed method.

Keywords: Residual stress, lattice structure topology optimization, fictitious domain method, modified inherent strain method, metal additive manufacturing

1. Introduction

After several decades, powder bed metal additive manufacturing (AM) has been among the most popular AM techniques to fabricate functional end-use component for various applications, such as aerospace, biomedical implant, mold manufacturing, etc. However, a serious weakness that prevents it from broad application is the residual stress inherent in the melting and solidification process [1-3]. In powder bed AM, the material in the build is melted and cooled several times, and stress is accumulated due to inconsistent level of heating [4]. This residual stress leads to severe problem because it can cause warpage, cracks, and delamination during processing, which may block the recoater blade and result in a build failure. Figure 1(a) illustrates such example of a failed build. The powder spreading is stopped as the built part delaminates from the building tray and deforms so significantly that it stops the powder recoater blade from moving. Such a build failure is very common in practice, which leads to a waste of manufacturing time and material consumption.

Another challenge of the residual stress is the large deformation after the part is removed from the build tray. Sometimes the part may not exhibit deformation during the printing processes, however, once it is cut from the substrate, residual stress is relaxed and deforms the component. This results in limited load resistance, dimensional inaccuracy, and reduction of the fatigue performance compared with the conventional bulk material [5, 6]. As illustrated in Fig. 1(b), an implant manufactured using Direct Metal Laser Sintering (DMLS) in Ti6Al4V shows undesirable deformation after removal from the build tray. For component with overhang or protruding features, refer to Fig. 1(c), the problem is even more challenging since residual stress tends to cause distortion and leads to severe warpage and damage at those areas.

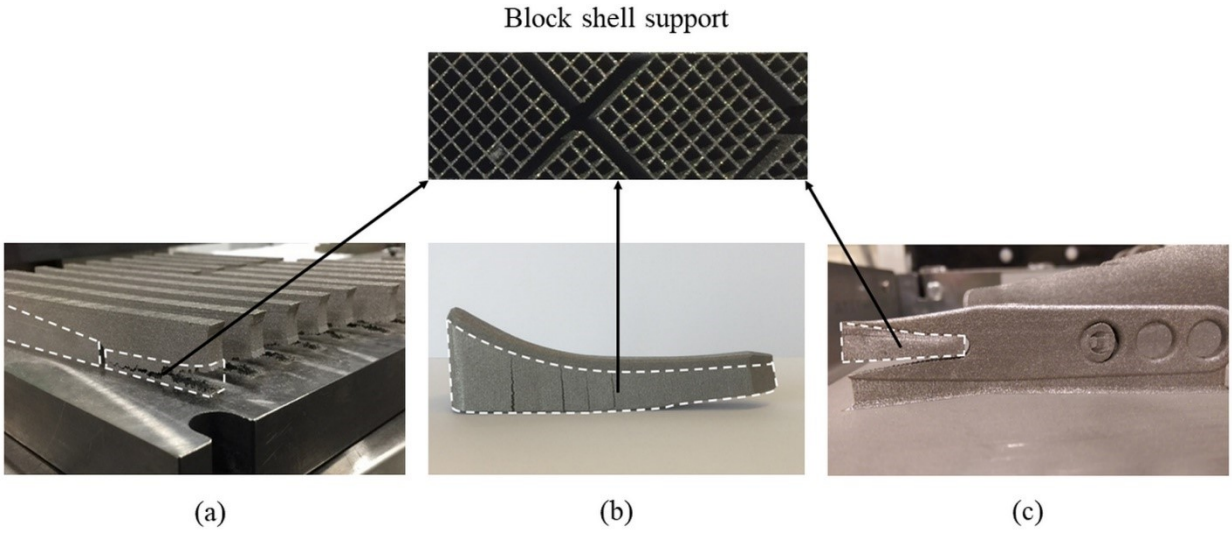

Fig. 1. Residual stress and large deformation of metal AM: (a) Bulk block with support structure before cutting from the building chamber; (b) implant with support structure after removal from the chamber; (c) component with protruding feature deformed during the manufacturing.

On the other hand, temporary support structures (e.g. block shell support highlighted by white dash line in Fig. 1) are generally added beneath the overhangs and simultaneously manufactured with the component. The support structure is used to provide mechanical fixture and heat dissipation channels to ensure manufacturability. Since the support structure is temporary and post-removed, it normally consists of uniform shell or scaffold structures [7] with lots of pores to reduce manufacturing time and costs. AM practitioners are typically designing support structures based on experiences to prevent

distortion/delamination caused by residual stresses, e.g., to adjust orientation or configuration of the support structure. It may be easy to design support for simple components, but for complex components, the empirical approach may not work, and many design iterations need to be taken to obtain a support structure that can ensure the entire build is manufacturable. This not only lengths the development of the product, but also leads to a waste of time and materials. Thus, an efficient physics-based design method needs to be developed to automatically optimize the design of support structure to ensure manufacturability of the component and minimize the mass of sacrificial support structure simultaneously.

There is a number of researches existing in the literature on support structure design for AM techniques. Allen et al. [8] proposed a methodology to optimize orientation of an object to minimize the support structure. Frank et al. [9] introduced an expert system-based selection strategy to find the preferred direction for rapid prototyping processes. Mumtaz et al. [10] depicted limitations of metal AM for the use of support structure and proposed some ways to eliminate support structure. Strano et al. [11] proposed a method to design support structure through the optimization of built orientation and cellular structure. Hussein et al. [7] applied the lattice structure with very low volume fraction for the design of support structure for DMLS technique. Calignano [12] gave an overview about the production of overhanging structures and applied Taguchi method to find the optimized orientation to minimize the amount of support surfaces. Recently, Vaidya et al. [13] presented an approach for minimizing support structures with space cellular infill in conjunction with Dijkstra's shortest path method to generate optimized support structure. Paul et al.[14] presented a voxel-based approach to minimize the support volume while minimizing the cylindricity and flatness errors of the part features. Das et al. [15, 16] proposed a method to minimize part errors in AM through the selection of build orientation for optimal support structures. However, most of these previous researches focus on geometric perspective for support structure design. Few works have been developed to treat residual stress of components manufactured by metal AM to guarantee the manufacturability through the optimization of support structure.

The aim of this work is to experimentally explore the feasibility of a support structure optimization framework for part-scale applications, in order to address the residual stress introduced build failure and guarantee the manufacturability. Instead of conducting detailed thermomechanical analysis, a modified inherent strain method [17, 18] is employed to calculate residual stress and simplify the computationally expensive process into a single-step structural analysis. This significantly reduces the computational cost from hours to minutes or seconds and makes it possible to use physics-based optimization for support structure design to reduce the maximum residual stress. The simulation is based on the hypothesis that the component is completely manufactured without residual stress release due to cracking or delamination. As the layer-by-layer manufacturing process progresses, larger amount of residual stress is accumulated in the component [19-21], and thus the maximum residual stress obtained from the as-built part is larger than any intermediate states. This ensures that the proposed optimization method is effective in preventing build failures illustrated in Fig. 1. On the other hand, delamination may also emerge in the new build layer due to the undesirably higher stress generated by transient heating and cooling [19, 20] cycle. The build failure due to this transient peak stress can be addressed by adjusting dwell time [19] and is left for the future work. To circumvent the error-prone mesh generation process, voxel-based mesh generation [14-16]is employed to discretize the domain of built part and support structure while a fictitious domain method (i.e. finite cell method) is employed to implement inherent strain method for residual stress calculation. In addition, lattice structure topology optimization method (LSTO) [22-25]is used to minimize volume of support structure under maximum stress constraint. By restricting the maximum stress under the yield strength, the introduced build failure is eliminated and deformation due to the residual stress is deceased. This not only reduces weight of sacrificial support structure but ensure the manufacturability of the component as well. The self-supporting and open-cell nature makes lattice structure a natural choice for support structure design,

since it can be printed out without support structure and also allows the trapped powder to be easily removed. To the best knowledge of the authors, this is the first work to apply topology optimization to design support structure for addressing build failure in powder-bed metal AM and experimentally study the performance.

The remaining content of this work is organized as follows. In Section 2, we describe the proposed support structure optimization framework for metal AM, which includes implementation of modified inherent strain method and LSTO method for support structure. Section 3 depicts the experimental study for two examples: one is the classic double cantilever beam while the other is a practical implant. Section 4 makes a conclusion for the examination of LSTO method for support structure design.

2. Design Optimization Methodology

2.1 Problem Formulation

The mathematical problem of optimizing the design of support structure for metal AM is described below. As shown in Fig. 2, suppose an AM part were to be built on a build tray with support structure underneath the long overhang. The entire domain can be divided into three sub domains: Build tray Ω_t, support structure Ω_s, and bulk component Ω_c. The bulk component is anchored onto the build tray by support structure. The goal of the optimization is to design the material distribution in support structure domain Ω_s to prevent residual stress induced build failure. Support structure has been widely used in metal AM techniques to provide mechanical fixture and heat dissipation to ensure manufacturability and is removed as sacrificial materials once AM builds are completed. Hence a reasonable objective for support design optimization is to minimize the overall mass of sacrificial support structure while constraining the maximum stress in domain Ω_s and Ω_c under the allowable stress. Note that the mass of the support domain will not completely vanish after optimization using the proposed objective. This is because the support domain connects the bulk component a build tray, and the bulk component is subjected to body loading of inherent strains, which remain unchanged during optimization. Hence the material distribution would tend to decrease from very high density near the bulk component toward lower density away from it. To reduce computation time in this optimization problem, we only consider the residual stress distribution after the entire part is done printing. The optimization is performed to iteratively update the density distribution in the support domain Ω_s until the stress constraint in domain $\Omega_s + \Omega_c$ is satisfied.

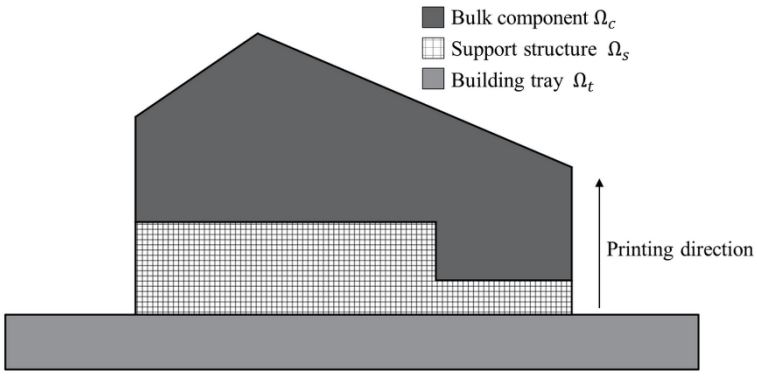

Fig. 2. Domain of an AM build

Based on the above discussion, the optimization problem for support structure design can be expressed mathematically as:

$$minimize \quad m(\boldsymbol{\rho}) = \sum_{e=1}^{N} \rho_e v_e \tag{1}$$

$$w.r.t \qquad \rho_e$$

$$such\ that \begin{cases} \mathbf{KU} = \mathbf{F}^{in} \\ \overline{\boldsymbol{C}} = \overline{\boldsymbol{C}}(\boldsymbol{\rho}) \\ \sigma_{max}^{H}(\boldsymbol{\rho}) \leq 1, \\ \underline{\rho} \leq \rho_e \leq \overline{\rho}, \quad e = 1, \dots, N \end{cases} \tag{2}$$

where $m(\boldsymbol{\rho})$ is the objective function of the optimization problem and represents the total mass of the support structure. $\mathbf{K}$, $\mathbf{U}$ and $\mathbf{F}^{in}$ in the equilibrium equation denote the stiffness matrix, global displacement and prescribed loading, respectively. ρ_e is the relative density of element e, and v_e is the corresponding elemental volume. The design variable ρ_e is limited by the upper bound $\overline{\rho}$ and lower bound $\underline{\rho}$. $\overline{\boldsymbol{C}} = \overline{\boldsymbol{C}}(\boldsymbol{\rho})$ represents elastic model of the support structure. σ_{max}^{H} denotes the maximum stress of the entire domain, and N is the number of elements in the support domain. Note that the stress measure in this work is given by the modified Hill criterion [26]. Without losing generality, the stress illustrated below is normalized by material's yield strength, which means that when the value of stress is larger than 1, plastic deformation occurs in the material, while when the stress is smaller than 1, the stress state is elastic. To solve the optimization problem in Eq. (1-2), the P-norm stress [27-30] is applied for the maximum residual stress constraint, the sensitivity analysis is performed for both objective function, and its constraints, and the Method of Moving Asymptotes (MMA) [31, 32] is employed to obtain the optimal design. Appendix please find the detailed derivation for P-norm stress measure and sensitivity analysis.

2.2 Inherent Strain Method for Residual Stress Estimation

The numerical solution of the optimization problem described in Eq. (1-2) usually needs hundreds of iterations to reach convergence and part-scale residual stress analysis is required in each iteration. The most accurate way for residual stress calculation is to employ a high-fidelity numerical model where the real powder melting, and solidification is simulated in detail according to the printing strategy. The accuracy of such detailed simulation method has been verified for prediction of temperature and deformation fields, as well as grain growth [33-37]. However, for part-scale problem, it is impractical to simulate residual stress by performing detailed process simulation (i.e. transient coupled thermomechanical simulation), which may take tens of hours for a simple geometry and make iterative optimization impossible. To circumvent the very high computational cost, the inherent strain method [38, 39] will be employed to efficiently compute residual stress/distortion for powder bed metal AM. The inherent strain method is originally proposed to efficiently simulate residual stress inherent in welding process. Due to the similarity of welding process with AM, the extension of the inherent strain method to rapidly simulate the residual stress distribution in AM part has drawn remarkable interest [40-45]. Keller et al. [42] proposed a multi-scale approach to extract inherent strain tensor components and implemented the inherent strain method by pure mechanical simulation. Good agreement was observed between computed distortion and experimental measure in Keller's [42] work. Li et al. [46] developed a multi-scale finite element model for fast prediction of distortion of parts manufactured by selective laser melting (SLM) process; however, no details were given on how to extract the inherent strain tensor in this work. Recently, Bugatti et al. [47] developed a finite element AM simulation based on the inherent strain method and discussed the limitations and strengths of inherent strain method for prediction of residual deformation in metal AM through experiments. Liang et al. [17, 43] proposed a modified inherent strain method for laser engineered net shaping (LENS) and conducted experiments to validate the predicted residual distortion. Setien et al. [48] presented an empirical methodology to determine inherent strains and validated it using the twin-cantilever beam made in Ti6Al4V alloy.

The prominent characterization of inherent strain method is that the computationally expensive thermo-mechanical simulation is replaced by a single static mechanical analysis. This makes it possible to conduct physics-based iterative optimization to systematically eliminate residual stress induced build failure. In this work, the method developed in Ref. [17, 42, 43, 48] is employed to extract the inherent strain vectors for powder-bed metal AM. With regard the implementation, the inherent strains are applied to both the support structure and bulk component as an equivalent body loading and a static analysis is performed to simulate residual stress in the AM build. Once the stress distribution is obtained, the optimization problem described in Eq. (1-2) is solved iteratively to reduce volume of support structure until the maximum residual stress constrain is satisfied.

2.3 Lattice Structure Topology Optimization for Support Structure Design

Another barrier concerning the support design optimization problem stated in Eq. (1-2) is that designs obtained by conventional topology optimization (TO) may include a large number of long overhangs and closed-void structures [49], which lead to manufacturability issues and trapped powders. To address these issues, graded lattice structure topology optimization (LSTO) is employed to design the support structure instead of conventional TO. The key feature of lattice structure is its self-supporting and open-celled nature when the bridge span and strut size are chosen appropriately for the AM process and material of interest. This makes lattice structure ideal for support structure design, since it can be printed out without support structure while the trapped powder can be easily removed. The LSTO method utilizes homogenized model to gain efficiency and has been applied to determine the layout of graded lattice structure for various problems, such as minimum compliance [25, 50], natural frequency [51], and heat conduction [23, 52]. As shown in Fig. 3, for a given component (illustrated in Fig. 3(a)), an overhang detection method [14, 15] is first applied to obtain support structure domain Ω_s for optimization. Instead of infilling the support structure domain with block shell support, variable-density lattice structure (see Fig. 3(b)) obtained from LSTO is used to provide mechanical fixture, dissipate heat, as well as ensure manufacturability. The details of the constrained stress optimization algorithm under the LSTO framework can be found in Ref. [53, 54] for interested readers. With regard overhang detection, this work categorizes overhang features into three groups: facet overhang, edge overhang, and point overhang, in order to determine the critical support structure domain accurately. For instance, in Fig. 3(d), the overhang edges on the bottom surface of the oriented component are automatically detected, and the corresponding lattice structure supports are generated after optimization.

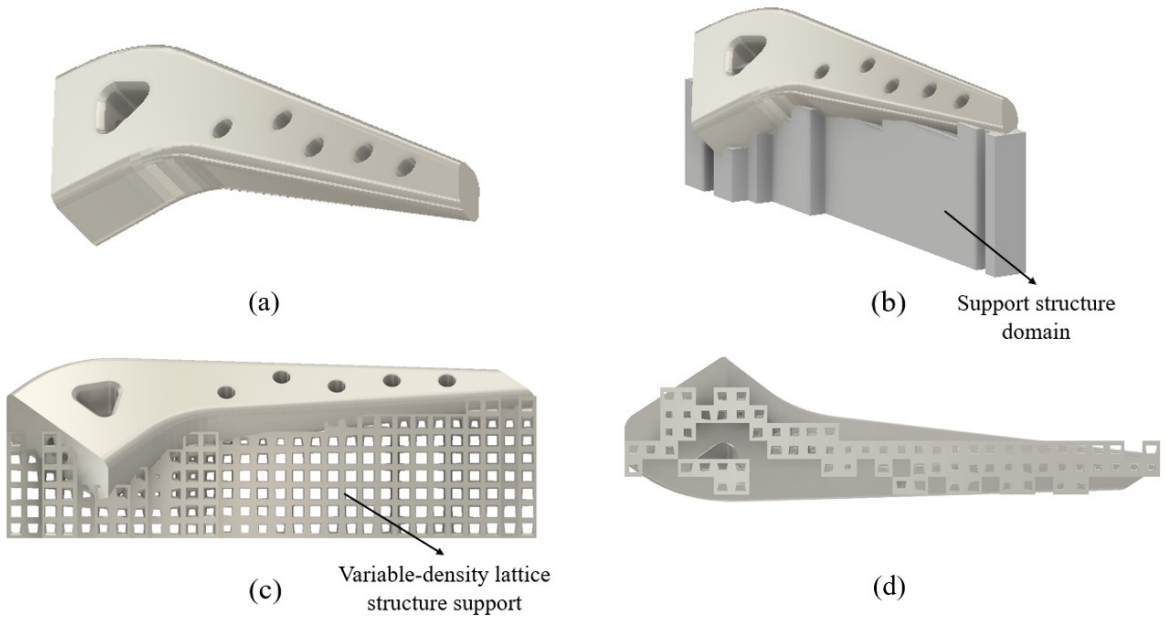

Fig. 3. Support structure design by the LSTO method: (a) Component, (b) component with bulk support, and (c) component with optimized variable-density lattice structure support, (d) bottom view of the optimized support structure for the component.

2.4 Finite Cell method for Implementation of Modified Inherent Strain Method

The unique feature of AM technology is its ability to manufacture geometrically complex components naturally with no additional tooling required. Nevertheless, mesh generation for such complex component and its support structure and build tray is computationally expensive and often error-prone. To simplify the mesh generation for complex geometry, the finite cell method (FCM) is employed to perform inherent strain-based analysis to obtain residual stress distribution for an AM build. The FCM, as a type of fictitious domain method, was first proposed by Parvizian et al [55] in 2007. The underlying principle of FCM [55-57] is to immerse the material domain of interest into a larger one, and a favorable Cartesian grid can thus be generated to avoid time-consuming and error-prone mesh generation. It has been successfully applied to solve a wide-range of problems, such as non-linear analysis [58], transport problem in porous media [59], biomechanical analysis [56, 60], etc.

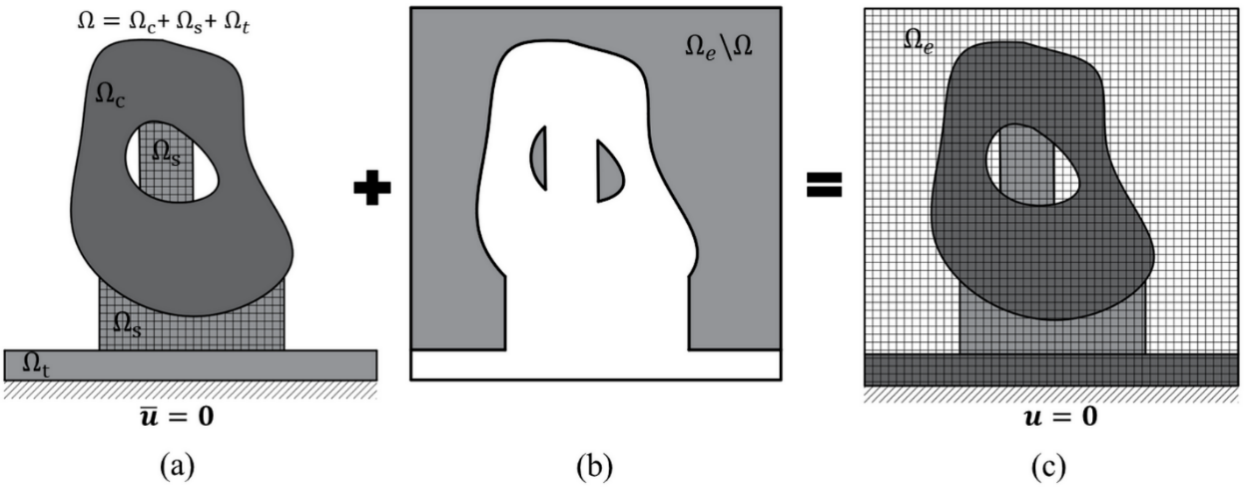

Fig. 4. The domain Ω in powder bed AM is embedded in a voxel-based domain Ω_e: (a) Domain of printed component, which is the combination by three subdomains: bulk component domain Ω_c, support structure domain Ω_s, and build tray domain Ω_t; (b) fictitious domain, and (c) embedding domain Ω_e.

In the context of inherent strain analysis of an AM build, the domain of the build shown in Fig. 2 is embedded into a larger domain based on FCM, and its boundary conditions are depicted in Fig. 4. The domain of computation Ω is the combination of three subdomains: Bulk component domain Ω_c, support structure domain Ω_s, and build tray domain Ω_t, and $\Omega = \Omega_c + \Omega_s + \Omega_t$. The physical domain Ω is embedded in a fictitious domain Ω_e with the boundary of $\partial\Omega_e$. The embedded boundary of Ω within Ω_e can be described as $\Gamma = \partial\Omega\ (\partial\Omega \cap \partial\Omega_e)$. For metal AM process, the bottom of build tray is fixed in place, and hence, the Dirichlet boundary $\overline{\boldsymbol{u}} = 0$ in domain Ω is directly extended to the embedded domain Ω_e. In the implementation, elements in the fictitious domain $\Omega_e \backslash \Omega$ is treated as a virtual material, whose elastic constants are set to small values to ensure robustness of the calculation, while for elements within the component domain Ω_c and support structure domain Ω_s, inherent strain vector is assigned as a body force in the analysis. It is noted that voxelization method proposed in Ref. [14] is employed to discretize the domains and generate the desired Cartesian mesh for FCM analysis.

Once the optimization based on FCM method is finished and the relative density is obtained, lattice reconstruction is performed to convert the density profile obtained from optimization into graded lattice structures. Figure 5 illustrates the reconstruction process for the support structure design. As can be seen in Fig. 5(b), for a given component, the voxel-based mesh is used to discretize the part and its support structure. The optimization problem proposed in Eq. (1-2) is solved by the method of moving asymptotes (MMA) [32] in order to optimize the relative density distribution in the support domain, refer to Fig. 5(c). After optimization, the relative density of the support structure is converted into variable-density lattice structure and combined with the solid component, which is then realized by AM.

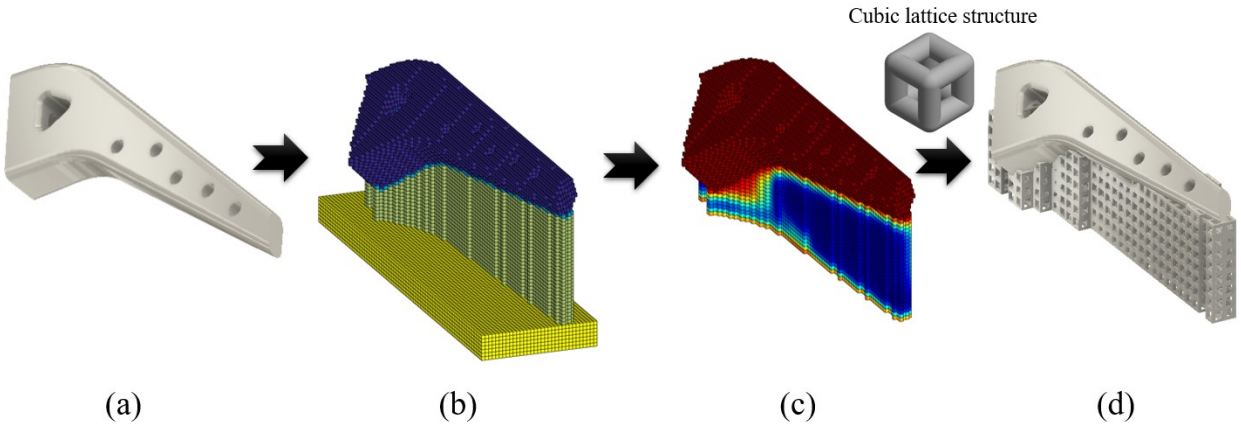

Fig. 5. Reconstruction process for a practical component. (a) Component for AM (b) voxel-based mesh for FCM analysis (c) optimal density profile of support domain (d) CAD model of component and optimal lattice support.

3. Numerical Example and Experimental Validation

The material of interest in this work is Ti6Al4V, which has Young's modulus of 110 GPa, Poisson's ratio of 0.3, and yield strength of 1140 MPa. As mentioned in Section 2, residual stresses described in the following discussions are normalized by yield strength in order to make it general for different materials. The inherent strain vector of Ti6Al4V used in this work is (-0.012, -0.012, 0.01), which is obtained using an in-house multiscale modeling code for laser powder bed metal AM based on the works in Refs. [17, 42, 43, 48]. Cubic lattice structure, as shown in Fig. 5, is used as the support material to anchor the solid component to the build tray. The homogenized elastic and yield models for the cubic lattice structure obtained in [61] are used to effectively describe its properties as a function of relative density in the support domain Ω_s. The relative density range of the support structure is set to be $\underline{\rho} = 0.2$ and $\bar{\rho} = 0.95$. The optimization is stopped when the change of volume fraction of the support structure within three successive iterations is smaller than 10^{-3}, while the stress constraint is satisfied. The voxel-based finite element analysis is implemented using Matlab R2016a.

3.1 Double Cantilever Beam Example

The first example is a classical double cantilever beam widely used as a benchmark to examine the accuracy of metal AM process simulation. Here, the model is applied to investigate the performance of the proposed support structure optimization method to prevent residual stress induced failure. The CAD model and voxel-based mesh for the double cantilever beam are illustrated in Fig. 6. The design domain for the support structure is the volume immediately under the overhanging beams. As illustrated in the figure, the dimension of the double cantilever beam is $80 \times 20 \times 24$ mm^3. The support domain on each side of the double cantilever beam is $36 \times 20 \times 15$ mm^3. The optimization aims to minimize support volume and at the same time restrict the maximum residual stress in the domain $\Omega_s + \Omega_c$ under the allowable stress. A mesh of 49,600 eight-node hexahedral elements of size 1 mm is applied to discretize the entire domain and solve the optimization problem. As illustrated in Fig. 6(b), the voxels of yellow color are for the support domain Ω_s, blue ones for the solid component Ω_c, and red ones for the substrate Ω_t. The thickness of the substrate is set to be 8 mm in the simulation. Note that in the simulation for residual stresses, a fixed boundary condition is subjected to the bottom of the substrate, while inherent strains are assigned to both the solid component and its support structure. For clarity, only the results in the domains of support structure

Ω_s and the domain of component Ω_c are plotted and shown in the discussion. The relative density of each element in the support domain is initially set to 0.9, while the elements in the component domain and substrate domain remain solid ($\rho = 1$) during the optimization.

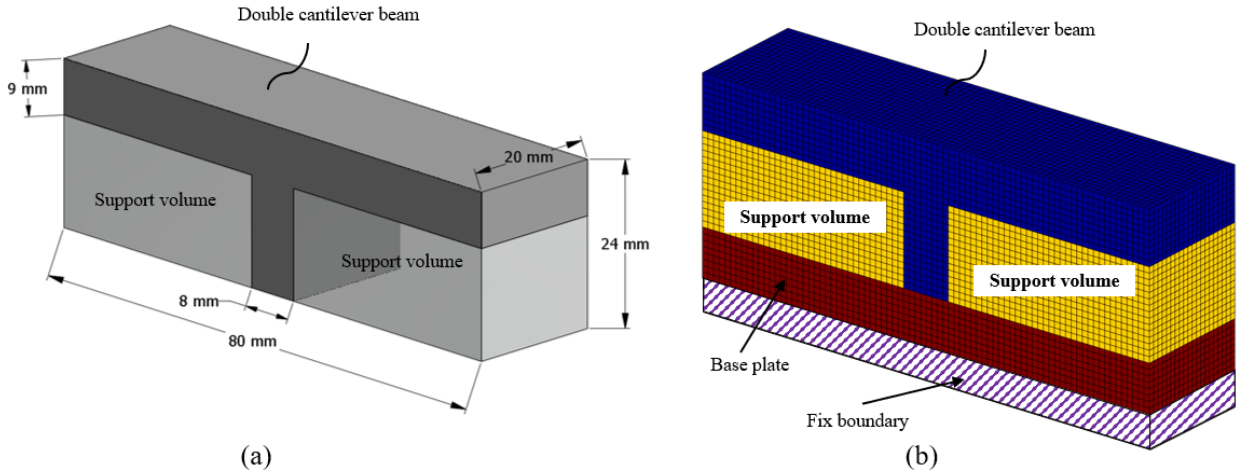

Fig. 6. CAD model and mesh model of double cantilever beam used for validation. (a) CAD model of the beam (b) voxel-based mesh model.

The optimization results are presented in Fig. 7 including the optimal density distribution, normalized stress distribution, and also the convergence history of the objective function and the normalized maximum residual stress. As can be seen in Fig. 7(c), the volume fraction of the support domain changes from 0.9 to 0.412 after 53 iterations (a 54.2% decrease), while the normalized maximum residual stress is decreased from 1.1 to 0.99, where unity indicates yielding. For the optimization results, the higher densities are mainly distributed around the upper corners of the beam, while lower densities are found far away from the center pillar. A number of intermediate densities (i.e. the yellow color area) exist in support domain between the high-density region and low-density region. The corresponding normalized stress after the optimization is given in Fig. 7(b). It can be observed that most of the normalized stresses within the support domain are smaller than 0.8. The larger stresses are distributed at the bottom surface of the center pillar, where the relative densities remain solid during optimization. The normalized maximum stress of the domain $\Omega_s + \Omega_c$ are smaller than yield strength, which theoretically ensures manufacturability of the build.

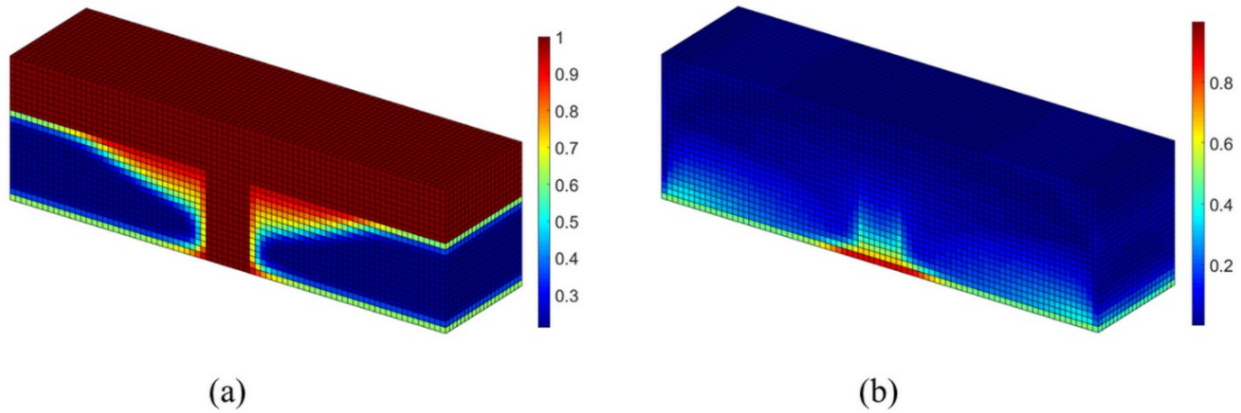

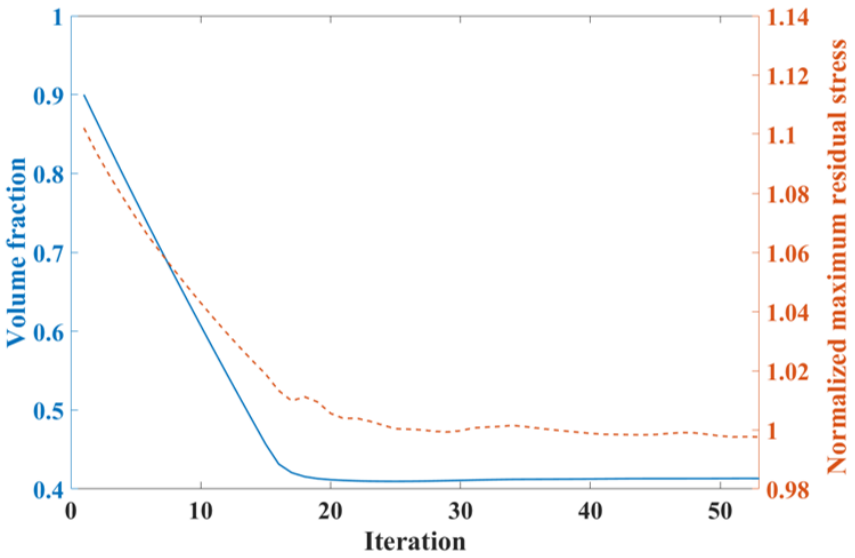

(c)

Fig. 7. Optimization results of the double cantilever beam: (a) Optimal density distribution (b) normalized residual stress distribution (c) convergence history.

For comparison purpose, the simulation is performed on uniform lattice structure of the same volume fraction or 0.412. The results are presented in Fig. 8. Compared with the optimal design, the normalized maximum stress of the uniform design is 1.09, which is larger than yield strength. The largest stresses are observed at the four bottom corners of the beam and the bottom surface of the center pillar.

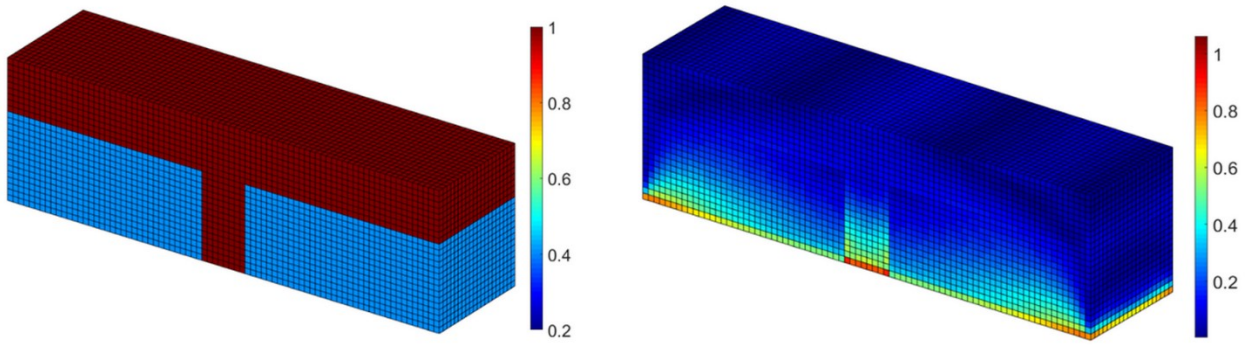

(a) (b)

Fig. 8. Simulation result of the design with uniform lattice structure: (a) Density distribution (b) normalized residual stress distribution.

To quantify performance of the optimal design, the double cantilever beams with four different support structures are designed and printed out for deformation measurement and comparison. Figure 9 illustrates the four different designs: i) Block shell support from Materialize Magics software (widely used in metal AM), ii) optimal variable-density lattice structure support, iii) uniform lattice structure support, and iv) teeth support. The volume fraction of the block shell support is 0.45, while the volume fraction of teeth support is 0.5.

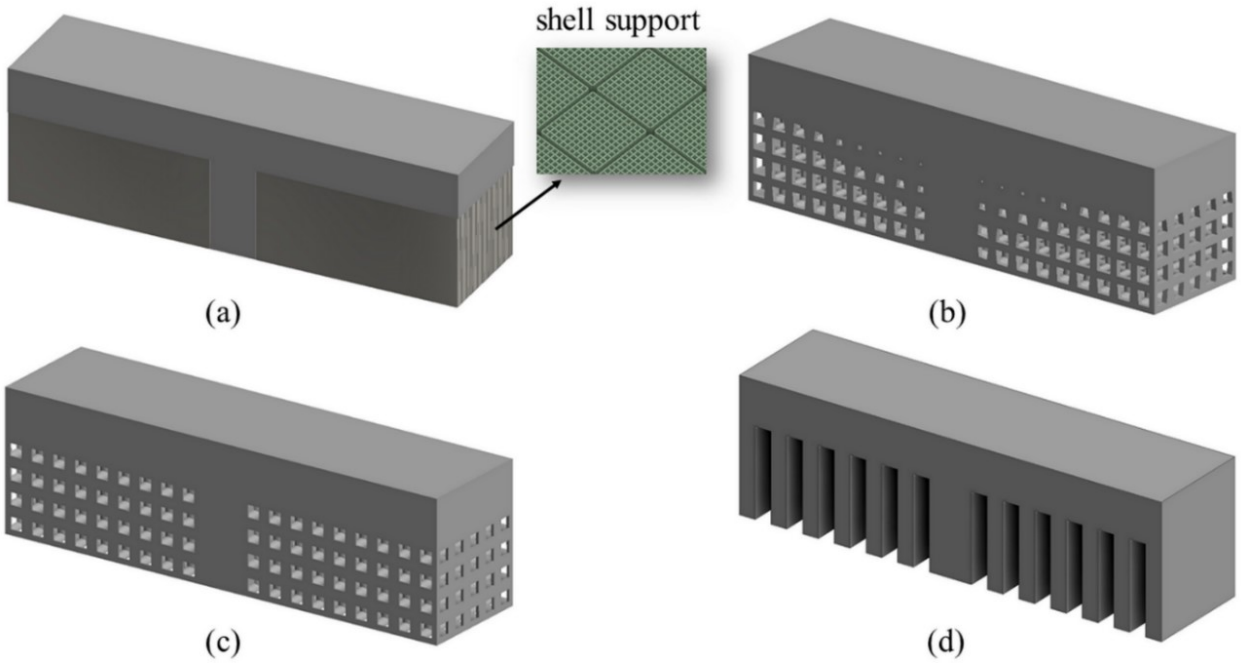

Fig. 9. Four different support structure designs for double cantilever beam for comparison purpose: (a) Shell support from Magic software (b) optimally variable-density lattice structure support (c) uniform lattice structure support, and (d) tooth support.

The four designs were printed out in Ti6Al4V on the same substrate and the photos are shown in Fig. 10. Due to cracking between support structure and build tray of the block shell style support, the beam is warped upward, which stops the powder recoater blade and results in a failed build. This demonstrates that the accumulation of residual stress inherent in the manufacturing process can lead to severe issue. One failed component can ruin the whole build and cause significant loss in time and costs. The failure not only lengths production of the component (i.e. designer needs to redesign the part), but also leads to a waste of material and time.

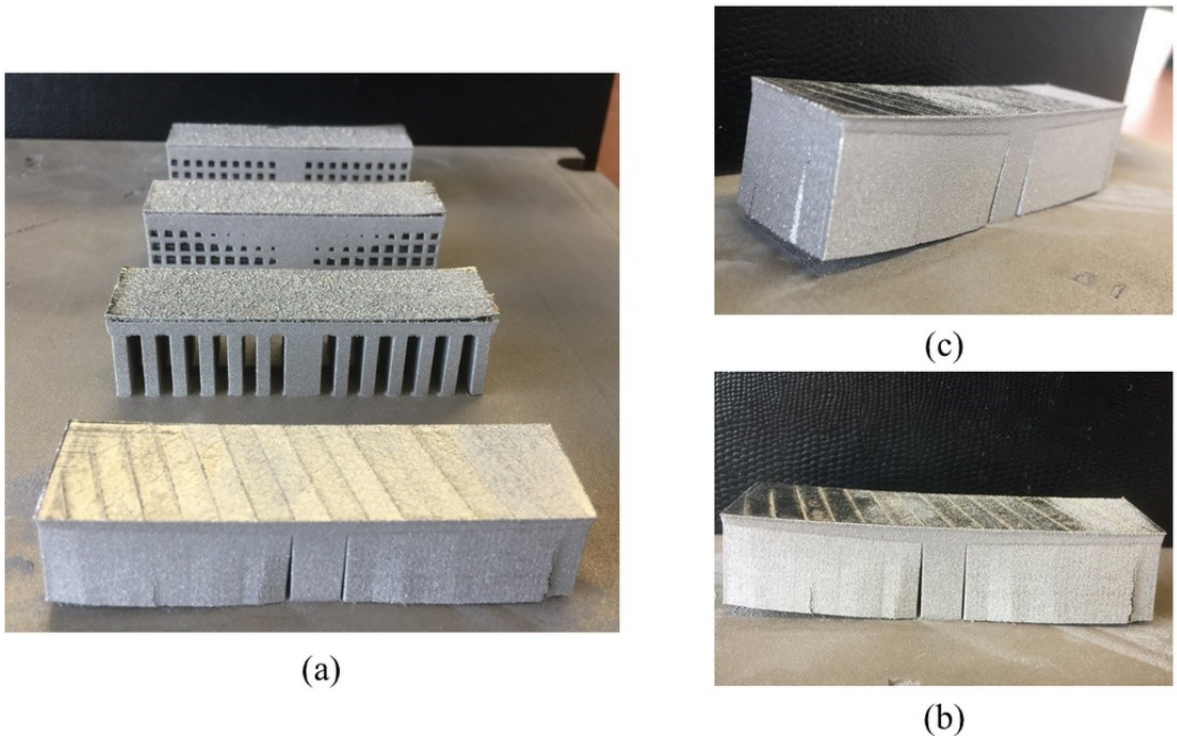

Fig. 10. Failed samples of the double cantilever beams printed out for validation: (a) Failed manufacturing due to large deformation formed by cracks between shell supports from Magic software and build tray. (b) and (c) Side view of the cracks for the first design.

To avoid build failure, the block shell support design was removed from the build and the remaining three beams were printed together in Ti6Al4V by the EOS DMLS. As shown in Fig. 11, although cracks are observed for the teeth support design, the build for the three beams were successful. Compared to the block shell support and teeth support, both the uniform lattice structure design and optimal lattice structure design were manufactured without observed cracking. This implies that the open-cell lattice structure can relieve residual stress effectively and can be used for support structure design for metal AM.

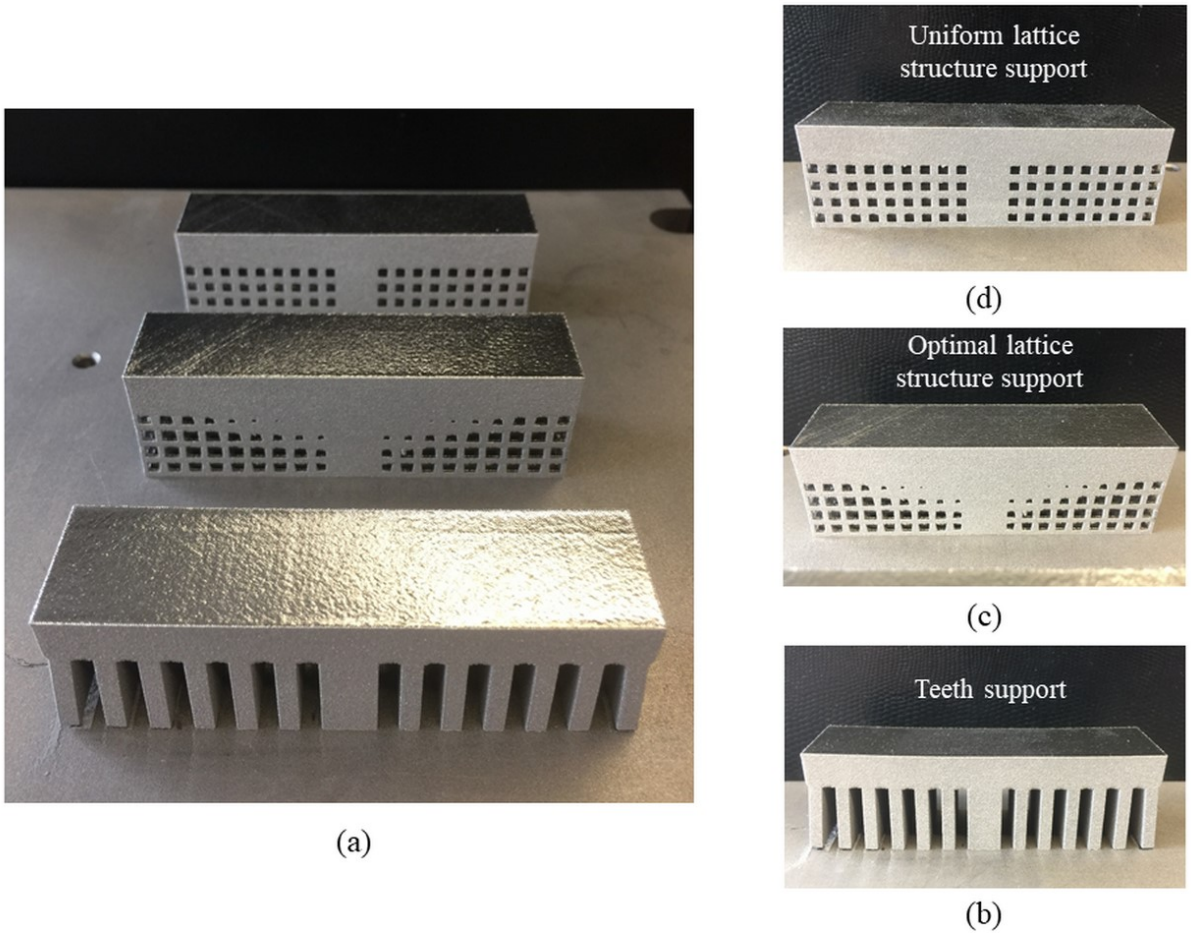

Fig. 11. Second build for samples of the double cantilever beam printed out by EOS DMLA in Ti6Al4V: (a) Photos of the three printed out beams for validation; (b) photo of the beam with teeth support (c) photo of the beam with optimal lattice structure support (d) photo of the beam with uniform lattice structure support.

In order to validate the effectiveness of the proposed method, one cantilever beam on either side was created by separating each from the support structure using a wire-cut EDM machine. The beams deflected upward as a result of stress relief from the cutting. A 3D scanning device Faro Laser ScanArm V3 (FARO Technologies) with an accuracy of 0.065 mm was employed to experimentally measure the deformation. Following scanning, the Geomagic software was used to process the data from the scan. The experimental apparatus, machined beams, and experimental results are shown in Fig. 12, respectively. The optimized beam exhibits the smallest deformation compared to the other two designs. The maximum deformation of the beam with the optimized support is 0.45 mm, while the other two structures have deflections larger than 1 mm. This demonstrates that the proposed method can significantly reduce the residual stresses inherent in the AM process. The method not only ensures manufacturability of the design (i.e. comparing with the block style support in Fig. 9), but also considerably enhances the quality of the bulk component (i.e. smaller deformation).

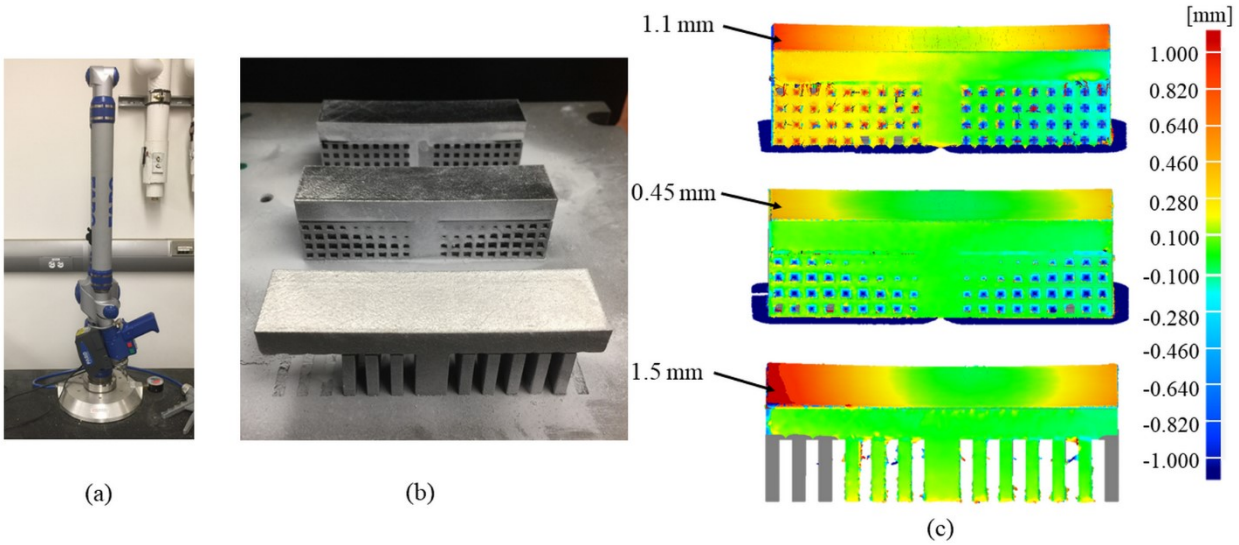

Fig. 12. Experimental measurement for the distortion of the beams after cut by electronic beam machining (EBM): (a) 3D laser scanning device Faro Laser ScanArm V3 made by FARO Technologies (b) photos of three beams after cut by EBM (c) deformation obtained by 3D scanning.

To further examine the performance of the optimized design, full-scale process simulations are performed on the three models in Fig. 11. The commercial software Simufact Additive v4.0 from MSC Inc. is employed to simulate residual distortion distribution and residual stress distribution. As shown in Fig. 13, the three beams are placed on a substrate of dimension $250 \times 250 \times 30$ mm^3. A fixed boundary condition is subjected to the bottom of the substrate. A voxel-based mesh of element size of 0.4 mm is used to discretize the design domain for simulation, refer to Fig. 13(b). The material of interest for both the beams and substrate is Ti6Al4V, which has a Young's modulus of 110 GPa, yield strength of 1140 MPa, tensile strength of 1340 MPa, and Poisson's ratio of 0.3.

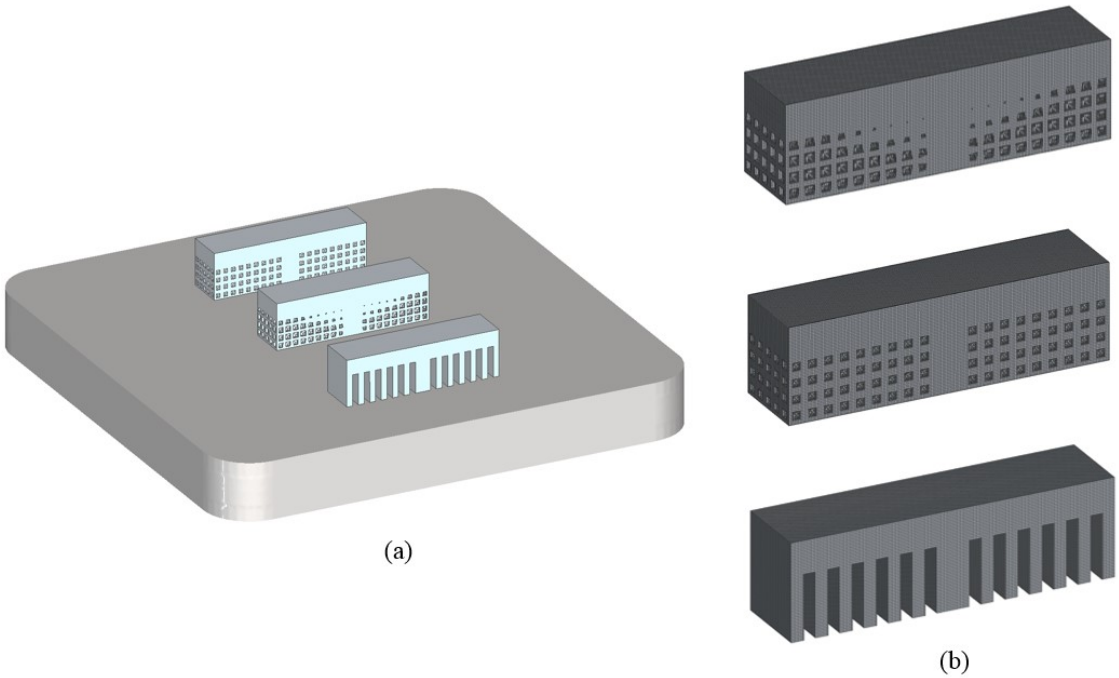

Fig. 13. CAD model and mesh for the full-scale simulation: (a) Setup of the beams on the substrate for simulation (b) voxel mesh for the full-scale simulation.

Figure 14 presents the simulation results containing both the total displacement and residual stress distribution for the three as-fabricated beams (i.e. before cutting). As illustrated in Fig. 14(a), larger distortions concentrate at the bottom outer edges of the beams near the support structure. Specifically, the optimal support design exhibits the smallest deformation (i.e., the maximum distortion is $u_{max} = 0.23$ mm) compared to uniform lattice support design, $u_{max} = 0.39$ mm, and teeth support design $u_{max} = 0.54$ mm. This is consistent with the observation in Fig. 11 and Fig. 12, in which shrinkage is found at the bottom side edges of the teeth support design. Figure 14(b) illustrates the residual stress distributions in the as-fabricated beams. As can be seen, the optimal lattice support design shows significantly smaller residual stresses than both uniform lattice support design and the teeth support design. Higher stresses are observed at the bottom areas of the teeth support. These higher stress regions cause delamination in the printed beam from the substrate, refer to Fig. 11(b). Among the three designs, the optimal lattice support shows the best overall control of residual stresses. This agrees well with the observation from the experimental measurement and proves that the proposed methodology is efficient in constraining residual stresses in components manufactured by powder-bed metal AM.

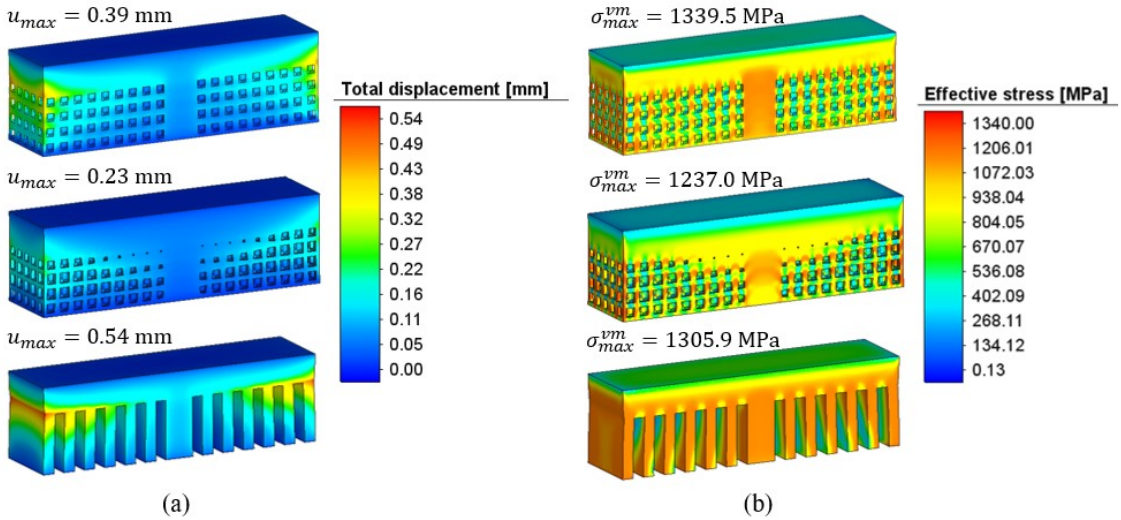

Fig. 14. Full-scale simulation results of the beams before cutting: (a) displacement distribution of the beams and (b) residual stress distribution of the beams.

3.2 Hip Implant Example

The second case is a typical hip implant used for bone replacement. The CAD model and dimension of the hip implant is shown in Fig. 15(a). The design envelope for the implant is $120 \times 35 \times 16$ mm^3. There are several bolt holes along the length of the implant used to fix the implant to human bone. The hip implant with the block style support structure was printed using the EOS M290 DMLS system in Ti6Al4V. However, as shown in Fig. 15(c) and (d), cracks and delamination from the build tray occurred during the AM process due to residual stress within the support structure and solid component. The cracking and delamination occurred certainly caused larger deformation of the build than otherwise, but they were not severe enough to cause a build failure. Another issue observed from this build is that the block shell style support structure trapped most of the powders since it is a closed-cell lattice structure. The trapped powders are difficult to remove post-build and lead to almost 100% waste of material in the support domain. On the other hand,

for open-celled lattice structure, the trapped powder can be easily removed and recycled for the next build, which results in much material and cost savings.

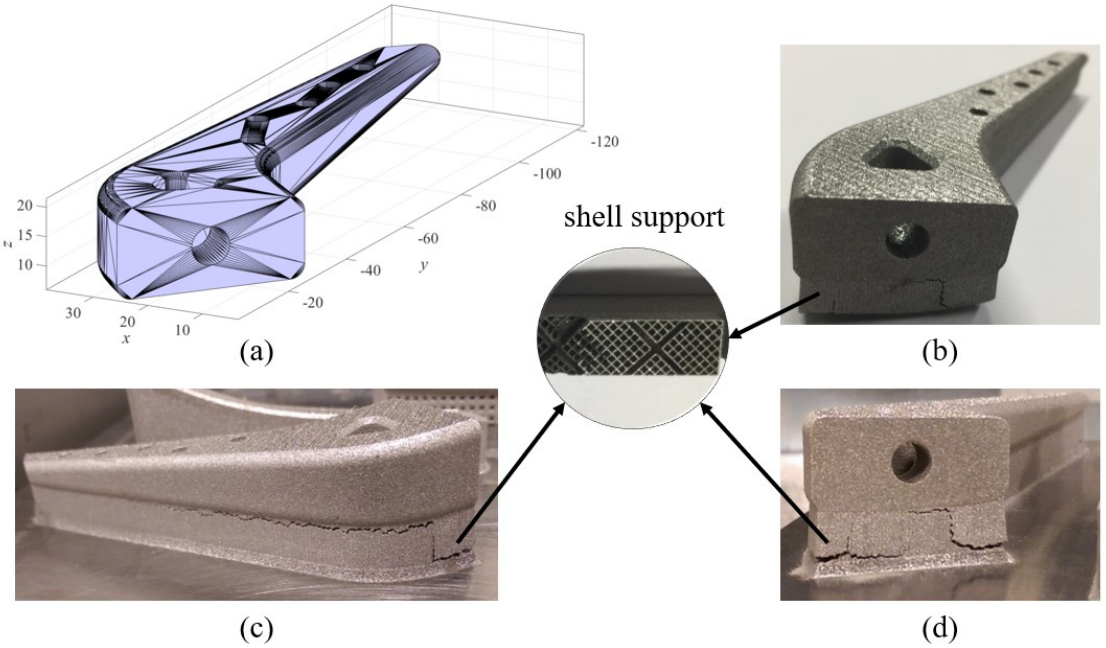

Fig. 15. CAD model of implant and its manufacturing in Ti6Al4V by EOS DMLS with shell support: (a) CAD model and dimension, (b) printed implant after cutting off from build tray, (c) left view of implant before cutting from the substrate, and (d) front view of implant before cutting from build tray.

In this case, the proposed methodology is employed to optimize the support structure for the hip implant to ensure a successful build. In particular, we use the optimization algorithm for the implant built in three different orientations, since different build orientations may lead to less support region and thus less effort for post-machining. As shown in Fig. 16, the implant is rotated about the *y*-axis by angles of 0°, 45°, and 90°, respectively, and is voxelized for both the part and its relevant support generated by the overhang detection proposed in Section 2. A uniform voxel-based mesh consisting of element size of 1 mm is employed to discretize the entire domain including the solid component, the support structure and the build tray. The thickness of the build tray here is identical to the former case, and the value is 8 mm, while the width and length of the base plate are determined by the bounding box of the part. The numbers of eight-node hexahedral elements used for the simulations are 97,329 for the orientation of 0°, 93,778 for 45°, and 75,607 for 90°, respectively; refer to Fig. 16(c), (f) and (i). In the simulation, the bottom surface of the base plate is fixed while the inherent strains are assigned to both the support structure domain Ω_s and bulk component domain Ω_c. The highlighted region in Fig. 16(a), (d) and (g) are the detected overhang features, while the yellow voxels in Fig. 16(b), (e) and (h) are the corresponding detected overhang voxels. The support volumes of these three orientations are computed by summing the number of support voxel to be: 1.602×10^4 mm^3, 1.064×10^4 mm^3 and 2.523×10^4 mm^3, respectively. It can be seen when the implant is rotated by an angle of 45°, the support volume is decreased by 5.38×10^3 mm^3 or 33.6% of the 0° angle case and by 1.459×10^4 mm^3 or 57.62% of the 90° case. This is because for angle 45°, the major detected overhangs are edge overhangs, and most of the facets at that angle satisfy the critical overhang requirement (i.e. the included angle by building direction is larger than 45°). This implies that the build orientation plays an important role in the design of support structure. For simplicity, only the results contain the distribution in domains of $\Omega_s + \Omega_c$ are plotted in the following discussion.

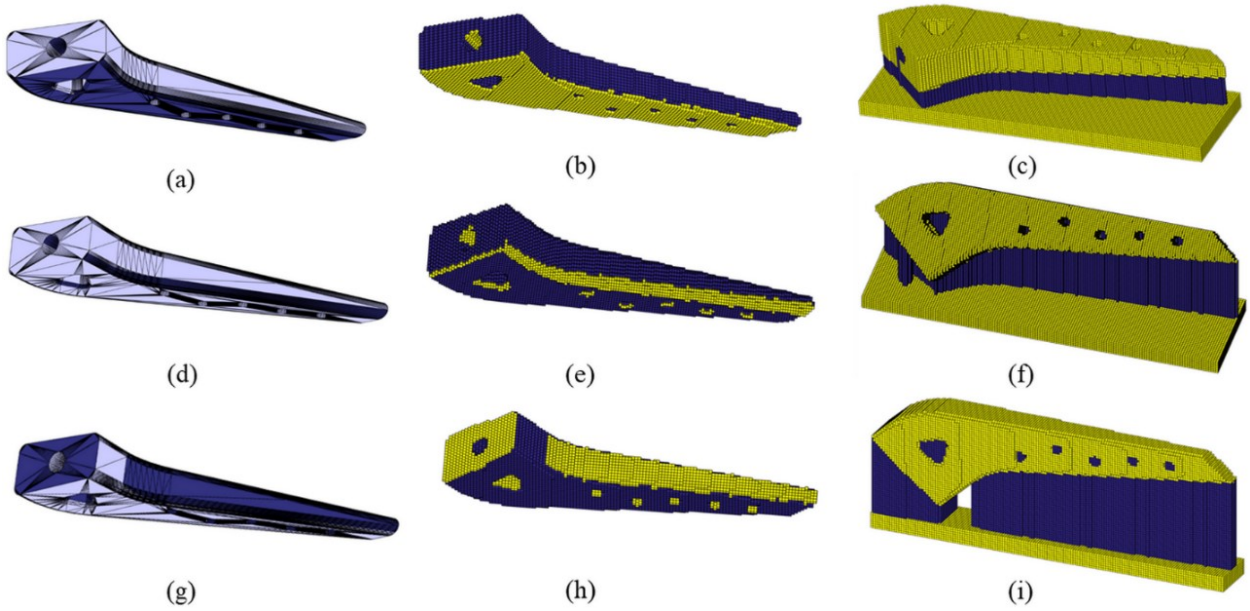

Fig. 16. Hip implant of different orientations: (a-c) STL file, voxelized part and Cartesian mesh for implant rotated by angle of 0°; (d-f) STL file, voxelized part and Cartesian mesh for implant rotated by angle of 45°; (g-i) STL file, voxelized part and Cartesian mesh for implant rotated by angle of 90°.

Table 1 Initial state of the optimization

	Orientation 0°	Orientation 45°	Orientation 90°
Support volume (mm^3)	1.602×10^4	1.064×10^4	2.523×10^4
Normalized maximum residual stress	3.1	2.42	2.12

The orientation of the component can also influence the stress distribution, especially the location of the stress concentration and maximum residual stress. As shown in Fig. 17, when the volume fraction of the support structure is set to 0.9, the large stresses mainly distribute at the interface between support structure and substrate, e.g., at the lower left and right corners of the three designs. These are the areas where cracking initiate and grow. Table 1 tabulates the support volume and the normalized maximum residual stress for the three cases. It can be seen that the part with no rotation (angle of 0°) has the largest normalized maximum stress, while the case with rotation angle of 90° case has the smallest value. This indicates that the orientation also has great influence on the stress distribution and magnitude of the maximum stress. The aim of this example is to explore the performance of the proposed methodology for the implant with different orientations.

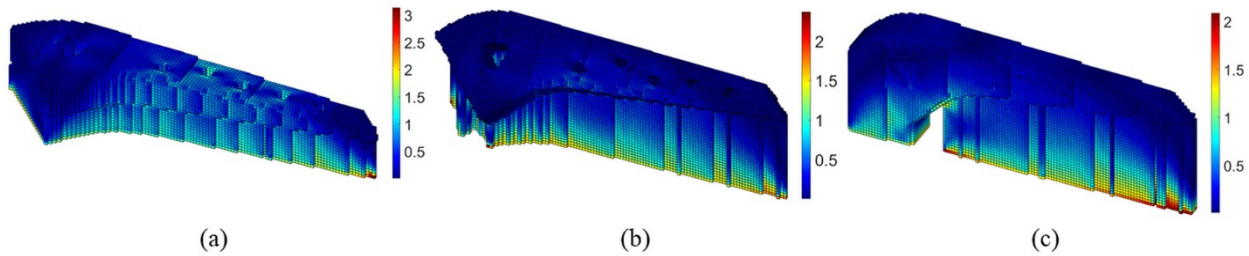

Fig. 17. Normalized residual stress distribution of hip implant with volume fraction of 0.9: (a) Oriented by angle of 0°, (b) oriented by angle of 45° and (c) oriented by angle of 90°.

The optimization results including the normalized stress profile, and relative density profile are given in Fig. 18. Table 2 tabulates the corresponding optimization results. For the 0° angle case, the volume fraction of the support structure converges from 0.9 to 0.41 after 60 iterations, and the normalized maximum residual stress is decreased to 0.82 from 3.1. For the 45° angle case, the volume fraction of the support structure is reduced to 0.36, and the normalized maximum residual stress is decreased to 0.91 after 73 iterations. In 64 iterations, the volume fraction for the final case of 90° angle converges to 0.46, and the normalized maximum stress is decreased to 0.81. The normalized maximum residual stresses in these three cases are optimized to below the yield strength and thus satisfy the imposed constraints after optimization.

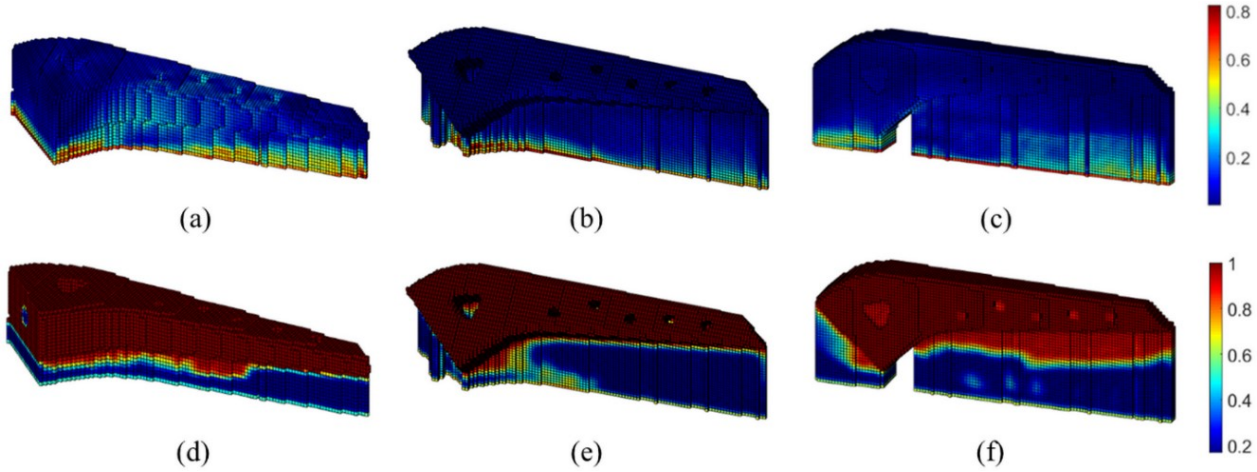

Fig. 18. Optimization results of the three orientations for hip implant: (a-c) Normalized residual stress distribution of the implant rotated by angle of 0°, 45° and 90°; (d-f) optimal density distribution of the implant rotated by angle of 0°, 45° and 90°.

Table 2 Optimization results of hip implant oriented by different degrees

	Orientation 0°	Orientation 45°	Orientation 90°
Volume fraction	0.41	0.36	0.46
Normalized maximum residual stress	0.82	0.91	0.81

The optimized densities shown in Fig. 18(d-f) are used to reconstruct the corresponding variable-density lattice structures, as illustrated in Fig. 19 in two different views. The contact areas between the component surface and support structure vary significantly as the implant is rotated at various angles. The angle of 45° exhibits the smallest contact area, which is consistent with the support volume calculated given in Table 1. The contact areas influence the cost of post-machining. Thus, among these three support designs, the orientation of 45° may require lower cost for post-machining.

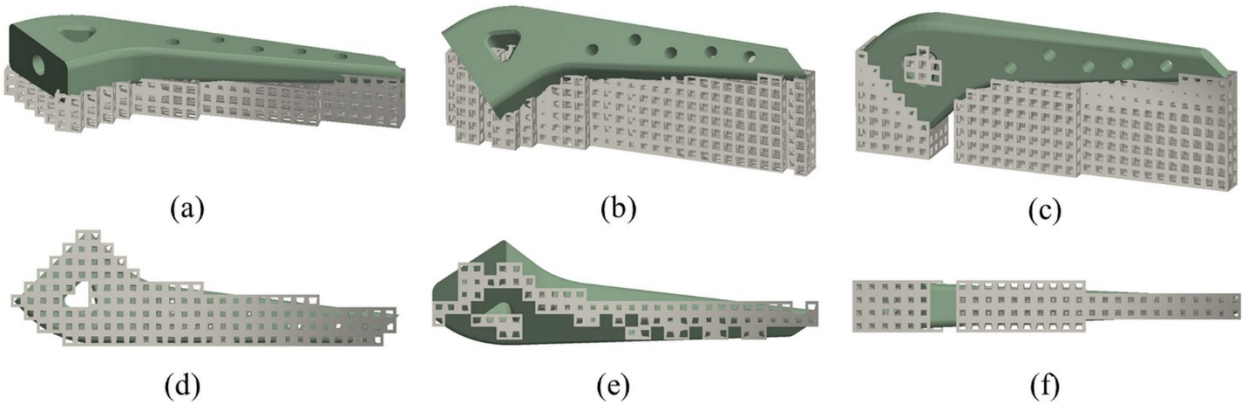

Fig. 19. Reconstruction of the optimal support structure design using variable-density lattice structure (a-c) Home-view of the implant rotated by angle of 0°, 45°and 90°; (d-f) bottom views of the three support structure designs.

For validation purpose, the three support structure designs for hip implant are printed out in Ti6Al4V and the photos are shown in Fig. 20. Compared with the un-optimized design shown in Fig. 15, the designs are successfully printed without obvious cracks. This demonstrates the effectiveness of the proposed methodology in constraining the residual stresses in an AM build. It also implies that the optimization framework can be efficiently employed for components with predefined orientations.

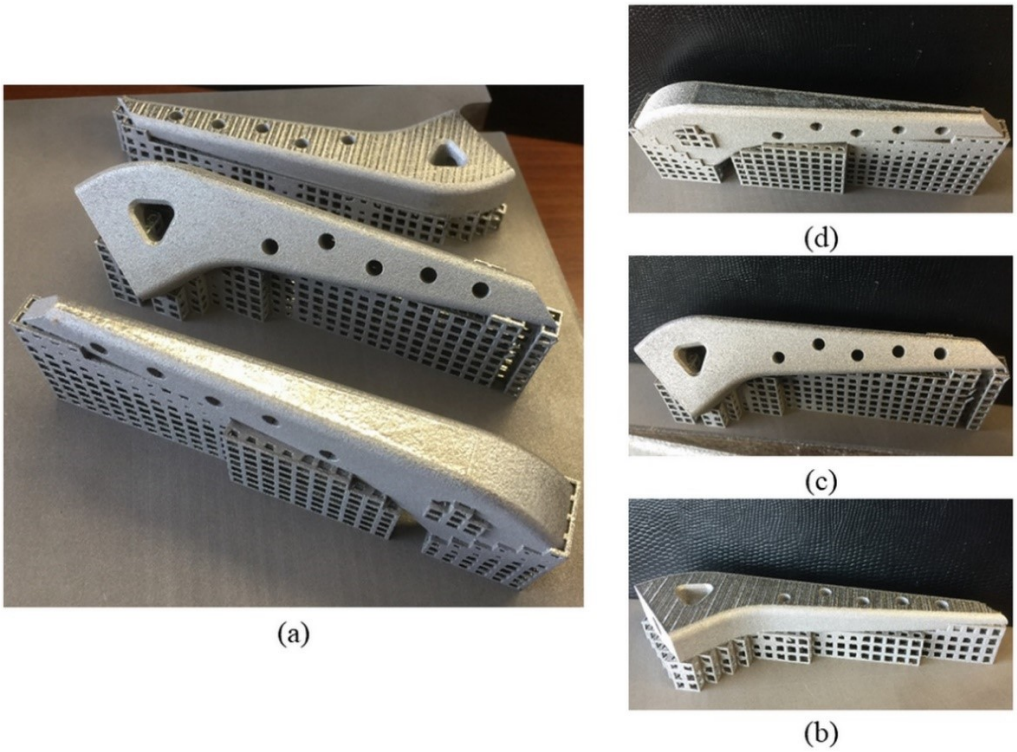

Fig. 20. Photos of the (a) printed implants at three different orientations with optimized graded lattice supports, (b) implant rotated by angle of 0° with its optimized support, (c) implant rotated by angle of 45° with its optimized support, and (d) implant rotated by angle of 90° with its optimized support. Note that there is no obvious cracking in all the designs.

4. Conclusion

The aim of this work is to experimentally examine the feasibility of part-scale optimization framework for support structure design, in order to address residual stress accumulation induced build failure in metal AM. The inherent strain method is employed to efficiently predict residual stress introduced by the powder melting and solidification process. The complex thermomechanical process, which normally requires very high computational cost, is simplified into a single-step static equilibrium analysis. This makes it possible to conduct optimization to iteratively solve the design problem involving residual stress. For the support structure, lattice structure is used as the support material due to its self-supporting and open-celled nature. The graded lattice structure topology optimization framework is proposed to iteratively minimize the sacrificial support structure under the maximum residual stress constraint. Several numerical examples are investigated to examine the performance of the optimization method. In the first example, the classical double cantilever beam structure is used to experimentally investigate the optimal design by comparing with a typical support design, teeth support design, and uniform lattice support design (same volume fraction as optimal design). By measuring the deformation after the beams are created by cutting, it is found that the optimal design can ensure the manufacturability of the design and also significantly reduce the residual stress (i.e. maximum deformation is reduced from 1.5 mm and 1.1 mm to 0.45 mm). The second example presents is a hip implant which also suffers from residual stress induced cracking. In that case, three different orientations are studied using the proposed optimization method and are printed out for validation. Although it is found that the orientation of the component has a significant influence on both the stress and support volume, the proposed methodology can optimize the design of support structure. Though visual inspection, the three designs for the implants are manufactured successfully without observed cracking. This further demonstrates the methodology can be effectively used to design industrial components for practical applications.

The optimization method assumes that the part is completely manufactured without cracking and delamination. This hypothesis ignores potential delamination caused by intermediate higher stress due to the transient steep thermal gradient. A rigorous study to understand the underlying principle of such build failure and develop a suitable optimization method to reduce the intermediate higher stress will be conducted in the future, in order to comprehensively overcome the build failure issue for additive manufacturing.

Although the proposed methodology can constrain the maximum residual stress and guarantee the manufacturability of the AM parts, the proposed method has not considered the post-removability of lattice structured supports by machining. The study for post-removability of the support lies in our future works. To address this issue, studies could be performed to minimize the support surfaces that are not accessible by post-machining through build orientation optimization or conduct optimization for support-free design. Alternatively, another method to remove the support structure is by using dissolvable support technique [62, 63], which utilizes a self-terminating chemical process to clean the support structure without destroying the original design. These topics should be explored in the future to take advantage of the simulation-based optimization to completely solve the issue of manufacturability and support post-removal for current powder-bed AM techniques.

Acknowledgements

The authors would like to acknowledge the financial support provided by the National Science Foundation (CMMI-1634261) and free trial license for Additive v4.0 software from Simufact MSC Inc.

Reference

[1] P. Mercelis and J.-P. Kruth, "Residual stresses in selective laser sintering and selective laser melting," *Rapid Prototyping Journal,* vol. 12, pp. 254-265, 2006.

[2] J.-P. Kruth, L. Froyen, J. Van Vaerenbergh, P. Mercelis, M. Rombouts, and B. Lauwers, "Selective laser melting of iron-based powder," *Journal of Materials Processing Technology,* vol. 149, pp. 616-622, 2004.

[3] L. Papadakis, A. Loizou, J. Risse, and J. Schrage, "Numerical computation of component shape distortion manufactured by selective laser melting," *Procedia CIRP,* vol. 18, pp. 90-95, 2014.

[4] A. E. Patterson, S. L. Messimer, and P. A. Farrington, "Overhanging Features and the SLM/DMLS Residual Stresses Problem: Review and Future Research Need," *Technologies,* vol. 5, p. 15, 2017.

[5] S. Leuders, M. Thöne, A. Riemer, T. Niendorf, T. Tröster, H. Richard*, et al.*, "On the mechanical behaviour of titanium alloy TiAl6V4 manufactured by selective laser melting: Fatigue resistance and crack growth performance," *International Journal of Fatigue,* vol. 48, pp. 300-307, 2013.

[6] E. O. t. Olakanmi, R. Cochrane, and K. Dalgarno, "A review on selective laser sintering/melting (SLS/SLM) of aluminium alloy powders: Processing, microstructure, and properties," *Progress in Materials Science,* vol. 74, pp. 401-477, 2015.

[7] A. Hussein, L. Hao, C. Yan, R. Everson, and P. Young, "Advanced lattice support structures for metal additive manufacturing," *Journal of Materials Processing Technology,* vol. 213, pp. 1019-1026, 2013/07// 2013.

[8] S. Allen and D. Dutta, "On the computation of part orientation using support structures in layered manufacturing," in *Proceedings of Solid Freeform Fabrication Symposium, University of Texas at Austin, Austin, TX, June*, 1994, pp. 259-269.

[9] D. Frank and G. Fadel, "Expert system-based selection of the preferred direction of build for rapid prototyping processes," *Journal of Intelligent Manufacturing,* vol. 6, pp. 339-345, 1995.

[10] K. Mumtaz, P. Vora, and N. Hopkinson, "A method to eliminate anchors/supports from directly laser melted metal powder bed processes," in *Proc. Solid Freeform Fabrication Symposium*, 2011, pp. 55-64.

[11] G. Strano, L. Hao, R. Everson, and K. Evans, "A new approach to the design and optimisation of support structures in additive manufacturing," *The International Journal of Advanced Manufacturing Technology,* vol. 66, pp. 1247-1254, 2013.

[12] F. Calignano, "Design optimization of supports for overhanging structures in aluminum and titanium alloys by selective laser melting," *Materials & Design,* vol. 64, pp. 203-213, 2014.

[13] R. Vaidya and S. Anand, "Optimum Support Structure Generation for Additive Manufacturing Using Unit Cell Structures and Support Removal Constraint," *Procedia Manufacturing,* vol. 5, pp. 1043-1059, 2016.

[14] R. Paul and S. Anand, "Optimization of layered manufacturing process for reducing form errors with minimal support structures," *Journal of Manufacturing Systems,* vol. 36, pp. 231-243, 2015.

[15] P. Das, K. Mhapsekar, S. Chowdhury, R. Samant, and S. Anand, "Selection of build orientation for optimal support structures and minimum part errors in additive manufacturing," *Computer-Aided Design and Applications,* pp. 1-13, 2017.

[16] P. Das, R. Chandran, R. Samant, and S. Anand, "Optimum part build orientation in additive manufacturing for minimizing part errors and support structures," *Procedia Manufacturing,* vol. 1, pp. 343-354, 2015.

[17] X. Liang, L. Cheng, Q. Chen, Q. Yang, and A. C. To, "A modified method for estimating inherent strains from detailed process simulation for fast residual distortion prediction of single-walled structures fabricated by directed energy deposition," *Additive Manufacturing,* vol. 23, pp. 471-486, 2018/10/01/ 2018.

[18] Y.-h. R. Tsai, "Rapid and accurate computation of the distance function using grids," *Journal of Computational Physics,* vol. 178, pp. 175-195, 2002.

[19] E. R. Denlinger, J. C. Heigel, P. Michaleris, and T. A. Palmer, "Effect of inter-layer dwell time on distortion and residual stress in additive manufacturing of titanium and nickel alloys," *Journal of Materials Processing Technology,* vol. 215, pp. 123-131, 2015/01/01/ 2015.
[20] T. Mukherjee, W. Zhang, and T. DebRoy, "An improved prediction of residual stresses and distortion in additive manufacturing," *Computational Materials Science,* vol. 126, pp. 360-372, 2017/01/01/ 2017.
[21] T. Mukherjee, J. Zuback, W. Zhang, and T. DebRoy, "Residual stresses and distortion in additively manufactured compositionally graded and dissimilar joints," *Computational Materials Science,* vol. 143, pp. 325-337, 2018.
[22] L. Cheng, J. Liu, X. Liang, and A. C. To, "Coupling lattice structure topology optimization with design-dependent feature evolution for additive manufactured heat conduction design," *Computer Methods in Applied Mechanics and Engineering,* vol. 332, pp. 408-439, 2018/04/15/ 2018.
[23] L. Cheng, J. Liu, and A. C. To, "Concurrent lattice infill with feature evolution optimization for additive manufactured heat conduction design," *Structural and Multidisciplinary Optimization,* January 30 2018.
[24] X. Duan, F. Li, and X. Qin, "Topology optimization of incompressible Navier–Stokes problem by level set based adaptive mesh method," *Computers & Mathematics with Applications,* vol. 72, pp. 1131-1141, 2016.
[25] L. Cheng, P. Zhang, E. Biyikli, J. Bai, J. Robbins, and A. To, "Efficient design optimization of variable-density cellular structures for additive manufacturing: theory and experimental validation," *Rapid Prototyping Journal,* vol. 23, 2017.
[26] L. Cheng, J. Bai, and A. C. To, "Functionally graded lattice structure topology optimization for the design of additive manufactured components with stress constraints," *Computer Methods in Applied Mechanics and Engineering,* 2018.
[27] M. W. Jones, J. A. Baerentzen, and M. Sramek, "3D distance fields: A survey of techniques and applications," *IEEE Transactions on visualization and Computer Graphics,* vol. 12, pp. 581-599, 2006.
[28] E. Holmberg, B. Torstenfelt, and A. Klarbring, "Stress constrained topology optimization," *Structural and Multidisciplinary Optimization,* vol. 48, pp. 33-47, 2013.
[29] J. París, F. Navarrina, I. Colominas, and M. Casteleiro, "Block aggregation of stress constraints in topology optimization of structures," *Advances in Engineering Software,* vol. 41, pp. 433-441, 2010.
[30] A. Sharma and K. Maute, "Stress-based topology optimization using spatial gradient stabilized XFEM," *Structural and Multidisciplinary Optimization,* October 24 2017.
[31] K. Svanberg, "MMA and GCMMA, versions September 2007," *Optimization and Systems Theory,* 2007.
[32] K. Svanberg, "The method of moving asymptotes—a new method for structural optimization," *International journal for numerical methods in engineering,* vol. 24, pp. 359-373, 1987.
[33] Q. Yang, P. Zhang, L. Cheng, Z. Min, M. Chyu, and A. C. To, "Finite element modeling and validation of thermomechanical behavior of Ti-6Al-4V in directed energy deposition additive manufacturing," *Additive Manufacturing,* vol. 12, pp. 169-177, 2016.
[34] W. Yan, S. Lin, O. L. Kafka, Y. Lian, C. Yu, Z. Liu*, et al.*, "Data-driven multi-scale multi-physics models to derive process–structure–property relationships for additive manufacturing," *Computational Mechanics,* pp. 1-21, 2018.
[35] B. Schoinochoritis, D. Chantzis, and K. Salonitis, "Simulation of metallic powder bed additive manufacturing processes with the finite element method: A critical review," *Proceedings of the Institution of Mechanical Engineers, Part B: Journal of Engineering Manufacture,* vol. 231, pp. 96-117, 2017.
[36] M. Masoomi, S. M. Thompson, and N. Shamsaei, "Laser powder bed fusion of Ti-6Al-4V parts: Thermal modeling and mechanical implications," *International Journal of Machine Tools and Manufacture,* vol. 118-119, pp. 73-90, 2017/08/01/ 2017.

[37] S. Shrestha and K. Chou, "A build surface study of Powder-Bed Electron Beam Additive Manufacturing by 3D thermo-fluid simulation and white-light interferometry," *International Journal of Machine Tools and Manufacture,* vol. 121, pp. 37-49, 2017/10/01/ 2017.
[38] H. Murakawa, D. Deng, N. Ma, and J. Wang, "Applications of inherent strain and interface element to simulation of welding deformation in thin plate structures," *Computational Materials Science,* vol. 51, pp. 43-52, 2012.
[39] M. Yuan and Y. Ueda, "Prediction of residual stresses in welded T-and I-joints using inherent strains," *Journal of engineering materials and technology,* vol. 118, pp. 229-234, 1996.
[40] S. Afazov, W. A. Denmark, B. L. Toralles, A. Holloway, and A. Yaghi, "Distortion prediction and compensation in selective laser melting," *Additive Manufacturing,* vol. 17, pp. 15-22, 2017.
[41] N. Ma, K. Nakacho, T. Ohta, N. Ogawa, A. Maekawa, H. Huang*, et al.*, "Inherent Strain Method for Residual Stress Measurement and Welding Distortion Prediction," in *ASME 2016 35th International Conference on Ocean, Offshore and Arctic Engineering*, 2016, pp. V009T13A001-V009T13A001.
[42] N. Keller and V. Ploshikhin, "New method for fast predictions of residual stress and distortion of AM parts."
[43] J. Luo, Z. Luo, L. Chen, L. Tong, and M. Y. Wang, "A semi-implicit level set method for structural shape and topology optimization," *Journal of Computational Physics,* vol. 227, pp. 5561-5581, 2008/05/10/ 2008.
[44] E. Salvati, A. Lunt, S. Ying, T. Sui, H. Zhang, C. Heason*, et al.*, "Eigenstrain reconstruction of residual strains in an additively manufactured and shot peened nickel superalloy compressor blade," *Computer Methods in Applied Mechanics and Engineering,* vol. 320, pp. 335-351, 2017.
[45] M. Fransen, "Eigenstrain reconstruction of residual stresses induced by selective laser melting," 2016.
[46] L. Cheng, X. Liang, E. Belski, X. Wang, J. M. Sietins, S. Ludwick*, et al.*, "Natural Frequency Optimization of Variable-Density Additive Manufactured Lattice Structure: Theory and Experimental Validation," *Journal of Manufacturing Science and Engineering,* vol. 140, p. 105002, 2018.
[47] C. Li, C. Fu, Y. Guo, and F. Fang, "Fast prediction and validation of part distortion in selective laser melting," *Procedia Manufacturing,* vol. 1, pp. 355-365, 2015.
[48] I. Setien, M. Chiumenti, S. van der Veen, M. San Sebastian, F. Garciandía, and A. Echeverría, "Empirical methodology to determine inherent strains in additive manufacturing," *Computers & Mathematics with Applications,* 2018.
[49] T. E. Johnson and A. T. Gaynor, "Three-dimensional Projection-based Topology Optimization for Prescribed-angle Self-Supporting Additively Manufactured Structures," *Additive Manufacturing,* 2018.
[50] L. Cheng, P. Zhang, E. Biyikli, J. Bai, S. Pilz, and A. C. To, "Integration of Topology Optimization with Efficient Design of Additive Manufactured Cellular Structures," 2015.
[51] L. Cheng, X. Liang, E. Belski, X. Wang, J. M. Sietins, S. Ludwick*, et al.*, "Natural Frequency Optimization of Variable-Density Additively Manufactured Lattice Structure: Theory and Experimental Validation," *Journal of Manufacturing Science and Engineering,* vol. In process, 2017.
[52] L. Cheng, J. Liu, X. Liang, and A. C. To, "Coupling Lattice Structure Topology Optimization with Design-Dependent Feature Evolution for Additive Manufactured Heat Conduction Design " *Computer Methods in Applied Mechanics and Engineering,* 2018.
[53] G. Barozzi and G. Pagliarini, "A method to solve conjugate heat transfer problems: the case of fully developed laminar flow in a pipe," *Journal of heat transfer,* vol. 107, pp. 77-83, 1985.
[54] M. Strantza, B. Vrancken, M. B. Prime, C. Truman, M. Rombouts, D. W. Brown*, et al.*, "Directional and oscillating residual stress on the mesoscale in additively manufactured Ti-6Al-4V," *Acta Materialia,* 2019/01/30/ 2019.

[55] J. Parvizian, A. Düster, and E. Rank, "Finite cell method," *Computational Mechanics,* vol. 41, pp. 121-133, 2007.
[56] M. Ruess, D. Tal, N. Trabelsi, Z. Yosibash, and E. Rank, "The finite cell method for bone simulations: verification and validation," *Biomechanics and modeling in mechanobiology,* vol. 11, pp. 425-437, 2012.
[57] A. Düster, J. Parvizian, Z. Yang, and E. Rank, "The finite cell method for three-dimensional problems of solid mechanics," *Computer methods in applied mechanics and engineering,* vol. 197, pp. 3768-3782, 2008.
[58] D. Schillinger, A. Düster, and E. Rank, "The hp‐d‐adaptive finite cell method for geometrically nonlinear problems of solid mechanics," *International Journal for Numerical Methods in Engineering,* vol. 89, pp. 1171-1202, 2012.
[59] Q. Cai, S. Kollmannsberger, R.-P. Mundani, and E. Rank, "The finite cell method for solute transport problems in porous media," in *Proceedings of the international conference on finite elements in flow problems*, 2011.
[60] Z. Yang, M. Ruess, S. Kollmannsberger, A. Düster, and E. Rank, "An efficient integration technique for the voxel‐based finite cell method," *International Journal for Numerical Methods in Engineering,* vol. 91, pp. 457-471, 2012.
[61] M. Langelaar, "Combined optimization of part topology, support structure layout and build orientation for additive manufacturing," *Structural and Multidisciplinary Optimization,* pp. 1-20, 2018.
[62] H. Zhao, "A fast sweeping method for eikonal equations," *Mathematics of computation,* vol. 74, pp. 603-627, 2005.
[63] R. Luciano and J. Willis, "Boundary-layer corrections for stress and strain fields in randomly heterogeneous materials," *Journal of the Mechanics and Physics of Solids,* vol. 51, pp. 1075-1088, 2003.
[64] J. D. Deaton and R. V. Grandhi, "Stress-based design of thermal structures via topology optimization," *Structural and Multidisciplinary Optimization,* vol. 53, pp. 253-270, 2016.
[65] C. Le, J. Norato, T. Bruns, C. Ha, and D. Tortorelli, "Stress-based topology optimization for continua," *Structural and Multidisciplinary Optimization,* vol. 41, pp. 605-620, 2010.
[66] E. Lee, K. A. James, and J. R. Martins, "Stress-constrained topology optimization with design-dependent loading," *Structural and Multidisciplinary Optimization,* vol. 46, pp. 647-661, 2012.
[67] J. D. Deaton and R. V. Grandhi, "Topology optimization of thermal structures with stress constraints," 2013.
[68] F. J. Ramírez-Gil, M. d. S. G. Tsuzuki, and W. Montealegre-Rubio, "Global finite element matrix construction based on a CPU-GPU implementation," *arXiv preprint arXiv:1501.04784,* 2015.
[69] S. Zhang, A. L. Gain, and J. A. Norato, "Stress-based topology optimization with discrete geometric components," *Computer Methods in Applied Mechanics and Engineering,* vol. 325, pp. 1-21, 2017/10/01/ 2017.
[70] K. Svanberg, "The method of moving a asymptotes--A new method for structural optimization," *International journal for numberical methods in engineering,* 1987.
[71] L. Cheng, J. Bai, and A. C. To, "Functionally graded lattice structure topology optimization for the design of additive manufactured components with stress constraints," *Computer Methods in Applied Mechanics and Engineering,* vol. 344, pp. 334-359, 2019/02/01/ 2019.

Appendix

1. P-norm stress measure

Following the work of [28, 64-67], P-norm stress is applied to approximate the maximum stress measure of the design domain

$$\bar{\sigma}_{max}^{H} = \max_{e=1,\cdots,N}(\bar{\sigma}_{e}^{H}) \leq 1 \tag{A1}$$

using the form of

$$\sigma^{PN} = (\sum_{e=1}^{N}(\bar{\sigma}_{e}^{H})^{P})^{\frac{1}{P}} \leq 1 \tag{A2}$$

where $\bar{\sigma}_{e}^{H}$ denotes the normalized stress of element e, $\bar{\sigma}_{max}^{H}$ is the normalized maximum residual stress, N represents the total number of elements in finite element analysis (FEA), P is the coefficient factor of P-norm and applied to control the smoothness of the approximation. When $P \to \infty$, formulation in Eq. (A2) approaches to the maximum stress, while when $P = 1$, the P-norm value is the average stress. In practical implementation, since P is a limited value and the control on the actual maximum stress is lacking. Hence, the adaptive scheme proposed in [65, 68, 69] is applied to Eq. (A2) as

$$\sigma^{PN} \leq \vartheta^{I} \tag{A3}$$

where ϑ is calculated iteratively, and I ($I \geq 1$) represents the iteration number.

$$\vartheta^{I} = \varsigma^{I}\frac{(\sigma^{PN})^{I}}{(\bar{\sigma}_{max}^{H})^{I}} \tag{A4}$$

where $\varsigma^{I} \in (0,1]$. When $\varsigma^{I} = 1$, Eq. (A3) is equal to Eq. (A1), the optimization converges to the optimal solution. In the optimization, $\varsigma^{I} = 0.5$, when ϑ^{I} oscillates between two successive iterations, otherwise $\varsigma^{I} = 1$.

2. Sensitivity Analysis

The optimization problem for designing support structure proposed in Eq. (1-2) is solved by the Method of Moving Asymptotes (MMA) proposed by Svanberg [70], in which the first order derivative of the objective function and constraints are required. The following gives the sensitivity analysis of objective function and stress constraints. The first derivative of the objective function is

$$\frac{\partial m(\boldsymbol{\rho})}{\partial \rho_e} = v_e \tag{A5}$$

The first order derivative of stress constraint to relative density in Eq. (2) is

$$\frac{\partial \sigma^{PN}}{\partial \rho_e} = \sum_{e=1}^{N}\frac{\partial \sigma^{PN}}{\partial \bar{\sigma}_{e}^{H}}\frac{\partial \bar{\sigma}_{e}^{H}}{\partial \rho_e} \tag{A6}$$

The first term in the right-hand side of Eq. (A6) can be calculated based on the P-norm proposed in [27] as:

$$\frac{\partial \sigma^{PN}}{\partial \bar{\sigma}_{e}^{H}} = (\sum_{e=1}^{N}(\bar{\sigma}_{e}^{H})^{P})^{\left(\frac{1}{P}-1\right)}(\bar{\sigma}_{e}^{H})^{(P-1)} \tag{A7}$$

The second derivative in the right-hand side of Eq. (A2) can be calculated as:

$$\begin{aligned}\frac{\partial \bar{\sigma}_{e}^{H}}{\partial \rho_e} &= \frac{\partial\left\{\left[(\bar{\boldsymbol{\varepsilon}}-\epsilon\boldsymbol{\varepsilon}^{in})^{T}\mathbb{R}(\bar{\boldsymbol{\varepsilon}}-\epsilon\boldsymbol{\varepsilon}^{in})\right]^{\frac{1}{2}}\right\}}{\partial \rho_e} = \frac{1}{2}\left[\left(\bar{\boldsymbol{\varepsilon}}-\epsilon\boldsymbol{\varepsilon}^{in}\right)^{T}\mathbb{R}\left(\bar{\boldsymbol{\varepsilon}}-\epsilon\boldsymbol{\varepsilon}^{in}\right)\right]^{-\frac{1}{2}}\frac{\partial\left[\left(\bar{\boldsymbol{\varepsilon}}-\epsilon\boldsymbol{\varepsilon}^{in}\right)^{T}\mathbb{R}\left(\bar{\boldsymbol{\varepsilon}}-\epsilon\boldsymbol{\varepsilon}^{in}\right)\right]}{\partial \rho_e} \\ &= \frac{1}{2\bar{\sigma}_{e}^{H}}\left(2\left(\bar{\boldsymbol{\varepsilon}}-\epsilon\boldsymbol{\varepsilon}^{in}\right)^{T}\mathbb{R}\frac{\partial(\bar{\boldsymbol{\varepsilon}}-\epsilon\boldsymbol{\varepsilon}^{in})}{\partial \rho_e} + \left(\bar{\boldsymbol{\varepsilon}}-\epsilon\boldsymbol{\varepsilon}^{in}\right)^{T}\frac{\partial \mathbb{R}}{\partial \rho_e}\left(\bar{\boldsymbol{\varepsilon}}-\epsilon\boldsymbol{\varepsilon}^{in}\right)\right)\end{aligned} \tag{A8}$$

where $\mathbb{R}$ is the tensor used to formulate yield strength of lattice structure by using the constitutive model and the yield strength tensor, which can be formulated as $\mathbb{R} = \overline{\boldsymbol{C}}^{\boldsymbol{T}}\mathbb{M}\overline{\boldsymbol{C}}$ and $\mathbb{M}$ represents the plastic constants matrix, and $\overline{\boldsymbol{C}}$ denotes the constitutive model. More details about these two matrixes refer to [71]. Since the macroscopic strain $\bar{\boldsymbol{\varepsilon}}$ can be expressed as $\bar{\boldsymbol{\varepsilon}} = \boldsymbol{B}\mathbf{U}$, where $\boldsymbol{B}$ denotes the strain-displacement matrix while $\mathbf{U}$ is the displacement vector. Thus, the first term in Eq. (A8) can be expressed as:

$$2\left(\bar{\boldsymbol{\varepsilon}}-\epsilon\boldsymbol{\varepsilon}^{in}\right)^{T}\mathbb{R}\frac{\partial\left(\bar{\boldsymbol{\varepsilon}}-\epsilon\boldsymbol{\varepsilon}^{in}\right)}{\partial \rho_e} = 2\left(\bar{\boldsymbol{\varepsilon}}-\epsilon\boldsymbol{\varepsilon}^{in}\right)^{T}\mathbb{R}\left(\frac{\partial(\boldsymbol{BU})}{\partial \rho_e} - \frac{\partial \epsilon}{\partial \rho_e}\boldsymbol{\varepsilon}^{in}\right)$$

$$= 2\left(\bar{\boldsymbol{\varepsilon}} - \epsilon\boldsymbol{\varepsilon}^{in}\right)^T \mathbb{R}\left(\boldsymbol{B}\frac{\partial \boldsymbol{U}}{\partial \rho_e} - \frac{\partial \epsilon}{\partial \rho_e}\boldsymbol{\varepsilon}^{in}\right) \tag{A9}$$

While the second term can be expressed as:

$$\left(\bar{\boldsymbol{\varepsilon}} - \epsilon\boldsymbol{\varepsilon}^{in}\right)^T \frac{\partial \mathbb{R}}{\partial \rho_e}\left(\bar{\boldsymbol{\varepsilon}} - \epsilon\boldsymbol{\varepsilon}^{in}\right) = \left(\bar{\boldsymbol{\varepsilon}} - \epsilon\boldsymbol{\varepsilon}^{in}\right)^T \left(2\overline{\boldsymbol{C}}^{\boldsymbol{T}}\mathbb{M}\frac{\partial \overline{\boldsymbol{C}}}{\partial \rho_e} + \overline{\boldsymbol{C}}^{\boldsymbol{T}}\frac{\partial \mathbb{M}}{\partial \rho_e}\overline{\boldsymbol{C}}\right)\left(\bar{\boldsymbol{\varepsilon}} - \epsilon\boldsymbol{\varepsilon}^{in}\right) \tag{A10}$$

Substituting Eq. (A9) and Eq. (A10) into Eq. (A8) yields

$$\frac{\partial \bar{\sigma}_e^H}{\partial \rho_e} = \frac{1}{2\bar{\sigma}_e^H}\left(2\left(\bar{\boldsymbol{\varepsilon}} - \epsilon\boldsymbol{\varepsilon}^{in}\right)^T \mathbb{R}\left(\boldsymbol{B}\frac{\partial \boldsymbol{U}}{\partial \rho_e} - \frac{\partial \epsilon}{\partial \rho_e}\boldsymbol{\varepsilon}^{in}\right) + \left(\bar{\boldsymbol{\varepsilon}} - \epsilon\boldsymbol{\varepsilon}^{in}\right)^T \left(2\overline{\boldsymbol{C}}^{\boldsymbol{T}}\mathbb{M}\frac{\partial \overline{\boldsymbol{C}}}{\partial \rho_e} + \overline{\boldsymbol{C}}^{\boldsymbol{T}}\frac{\partial \mathbb{M}}{\partial \rho_e}\overline{\boldsymbol{C}}\right)\left(\bar{\boldsymbol{\varepsilon}} - \epsilon\boldsymbol{\varepsilon}^{in}\right)\right) \tag{A11}$$

Substituting Eq. (A7) and Eq. (A11) into Eq. (A6), the sensitivity of the *P*-norm stress can be computed as:

$$\begin{aligned}\frac{\partial \sigma^{PN}}{\partial \rho_e} &= \sum_{e=1}^{N}\left\{\left(\sum\nolimits_{e=1}^{N}(\bar{\sigma}_e^H)^P\right)^{\left(\frac{1}{P}-1\right)}(\bar{\sigma}_e^H)^{(P-1)}\left[\frac{1}{2\bar{\sigma}_e^H}\left(2\left(\bar{\boldsymbol{\varepsilon}} - \epsilon\boldsymbol{\varepsilon}^{in}\right)^T \mathbb{R}\left(\boldsymbol{B}\frac{\partial \mathbf{U}}{\partial \rho_e} - \frac{\partial \epsilon}{\partial \rho_e}\boldsymbol{\varepsilon}^{in}\right)\right.\right.\right.\\ &\left.\left.\left. + \left(\bar{\boldsymbol{\varepsilon}} - \epsilon\boldsymbol{\varepsilon}^{in}\right)^T \left(2\overline{\boldsymbol{C}}^{\boldsymbol{T}}\mathbb{M}\frac{\partial \overline{\boldsymbol{C}}}{\partial \rho_e} + \overline{\boldsymbol{C}}^{\boldsymbol{T}}\frac{\partial \mathbb{M}}{\partial \rho_e}\overline{\boldsymbol{C}}\right)\left(\bar{\boldsymbol{\varepsilon}} - \epsilon\boldsymbol{\varepsilon}^{in}\right)\right)\right]\right\}\\ &= \sum_{e=1}^{N}\left[\left(\sum\nolimits_{e=1}^{N}(\bar{\sigma}_e^H)^P\right)^{\left(\frac{1}{P}-1\right)}(\bar{\sigma}_e^H)^{(P-2)}\left(\bar{\boldsymbol{\varepsilon}} - \epsilon\boldsymbol{\varepsilon}^{in}\right)^T \mathbb{R}\left(\boldsymbol{B}\frac{\partial \mathbf{U}}{\partial \rho_e} - \frac{\partial \epsilon}{\partial \rho_e}\boldsymbol{\varepsilon}^{in}\right)\right]\\ &+ \frac{1}{2}\sum_{e=1}^{N}\left[\left(\sum\nolimits_{e=1}^{N}(\bar{\sigma}_e^H)^P\right)^{\left(\frac{1}{P}-1\right)}(\bar{\sigma}_e^H)^{(P-2)}\left(\bar{\boldsymbol{\varepsilon}} - \epsilon\boldsymbol{\varepsilon}^{in}\right)^T \left(2\overline{\boldsymbol{C}}^{\boldsymbol{T}}\mathbb{M}\frac{\partial \overline{\boldsymbol{C}}}{\partial \rho_e} + \overline{\boldsymbol{C}}^{\boldsymbol{T}}\frac{\partial \mathbb{M}}{\partial \rho_e}\overline{\boldsymbol{C}}\right)\left(\bar{\boldsymbol{\varepsilon}} - \epsilon\boldsymbol{\varepsilon}^{in}\right)\right]\end{aligned} \tag{A12}$$

Based on the equilibrium equation, the derivative of $\frac{\partial \mathbf{U}}{\partial \rho_e}$ can be calculated using the equilibrium equation as:

$$\frac{\partial \mathbf{U}}{\partial \rho_e} = \mathbf{K}^{-1}\frac{\partial \mathbf{F}^{in}}{\partial \rho_e} - \mathbf{K}^{-1}\frac{\partial \mathbf{K}}{\partial \rho_e}\mathbf{U} \tag{A13}$$

Substituting Eq. (A13) into the first term of Eq. (A12), one can obtain

$$\begin{aligned}\frac{\partial \sigma^{PN}}{\partial \rho_e} &= \sum_{e=1}^{N}\left[\left(\sum_{e=1}^{N}(\bar{\sigma}_e^H)^P\right)^{\left(\frac{1}{P}-1\right)}(\bar{\sigma}_e^H)^{(P-2)}\left(\bar{\boldsymbol{\varepsilon}} - \epsilon\boldsymbol{\varepsilon}^{in}\right)^T \mathbb{R}\left(\boldsymbol{B}\mathbf{K}^{-1}\left(\frac{\partial \mathbf{F}^{in}}{\partial \rho_e} - \frac{\partial \mathbf{K}}{\partial \rho_e}\mathbf{U}\right) - \frac{\partial \epsilon}{\partial \rho_e}\boldsymbol{\varepsilon}^{in}\right)\right]\\ &+ \frac{1}{2}\sum_{e=1}^{N}\left[\left(\sum_{e=1}^{N}(\bar{\sigma}_e^H)^P\right)^{\left(\frac{1}{P}-1\right)}(\bar{\sigma}_e^H)^{(P-2)}\left(\bar{\boldsymbol{\varepsilon}} - \epsilon\boldsymbol{\varepsilon}^{in}\right)^T \left(2\overline{\boldsymbol{C}}^{\boldsymbol{T}}\mathbb{M}\frac{\partial \overline{\boldsymbol{C}}}{\partial \rho_e} + \overline{\boldsymbol{C}}^{\boldsymbol{T}}\frac{\partial \mathbb{M}}{\partial \rho_e}\overline{\boldsymbol{C}}\right)\left(\bar{\boldsymbol{\varepsilon}} - \epsilon\boldsymbol{\varepsilon}^{in}\right)\right]\end{aligned} \tag{A14}$$

An adjoint variable $\boldsymbol{\lambda}$ is introduced to solve the sensitivity of the first term, and its definition is

$$\boldsymbol{\lambda}^{\boldsymbol{T}} = \sum_{e=1}^{N}\left(\sum_{e=1}^{N}(\bar{\sigma}_e^H)^P\right)^{\left(\frac{1}{P}-1\right)}(\bar{\sigma}_e^H)^{(P-2)}\left(\bar{\boldsymbol{\varepsilon}} - \epsilon\boldsymbol{\varepsilon}^{in}\right)^T \mathbb{R}\boldsymbol{B}\mathbf{K}^{-1} \tag{A15}$$

The adjoint variable $\boldsymbol{\lambda}$ can thus be computed by solving the following adjoint equation

$$\mathbf{K}\boldsymbol{\lambda} = \sum_{e=1}^{N}\left(\sum_{e=1}^{N}(\bar{\sigma}_e^H)^P\right)^{\left(\frac{1}{P}-1\right)}(\bar{\sigma}_e^H)^{(P-2)}\mathbb{R}\boldsymbol{B}\left(\bar{\boldsymbol{\varepsilon}} - \epsilon\boldsymbol{\varepsilon}^{in}\right) \tag{A16}$$

Once the adjoint variable is obtained, the sensitivity of the *P*-norm stress constraint in Eq. (A14) yields

$$\begin{aligned}\frac{\partial \sigma^{PN}}{\partial \rho_e} &= \boldsymbol{\lambda}^{\boldsymbol{T}}\left(\frac{\partial \mathbf{F}^{in}}{\partial \rho_e} - \frac{\partial \mathbf{K}}{\partial \rho_e}\mathbf{U}\right) - \sum_{e=1}^{N}\left[\left(\sum_{e=1}^{N}(\bar{\sigma}_e^H)^P\right)^{\left(\frac{1}{P}-1\right)}(\bar{\sigma}_e^H)^{(P-2)}\left(\bar{\boldsymbol{\varepsilon}} - \epsilon\boldsymbol{\varepsilon}^{in}\right)^T \mathbb{R}\frac{\partial \epsilon}{\partial \rho_e}\boldsymbol{\varepsilon}^{in}\right]\\ &+ \frac{1}{2}\sum_{e=1}^{N}\left[\left(\sum_{e=1}^{N}(\bar{\sigma}_e^H)^P\right)^{\left(\frac{1}{P}-1\right)}(\bar{\sigma}_e^H)^{(P-2)}\left(\bar{\boldsymbol{\varepsilon}} - \epsilon\boldsymbol{\varepsilon}^{in}\right)^T \left(2\overline{\boldsymbol{C}}^{\boldsymbol{T}}\mathbb{M}\frac{\partial \overline{\boldsymbol{C}}}{\partial \rho_e} + \overline{\boldsymbol{C}}^{\boldsymbol{T}}\frac{\partial \mathbb{M}}{\partial \rho_e}\overline{\boldsymbol{C}}\right)\left(\bar{\boldsymbol{\varepsilon}} - \epsilon\boldsymbol{\varepsilon}^{in}\right)\right]\end{aligned} \tag{A17}$$

The sensitivities in Eqs. (A5) and (A17) are implemented in the MMA method and are used for the lattice structure topology optimization for support structure design.